TURUN YLIOPISTON JULKAISUJA
ANNALES UNIVERSITATIS TURKUENSIS

SARJA - SER. A I OSA - TOM. 395

ASTRONOMICA - CHEMICA - PHYSICA - MATHEMATICA

USE OF THE OPTICAL CANTILEVER MICROPHONE IN PHOTOACOUSTIC SPECTROSCOPY

by

Juho Uotila

TURUN YLIOPISTO
Turku 2009

From the Laboratory of Optics and Spectroscopy
Department of Physics and Astronomy
University of Turku
Turku, Finland

Supervised by

Professor Jyrki Kauppinen
Department of Physics and Astronomy
University of Turku
Turku, Finland

Reviewed by

Professor Risto Myllylä
Department of Electrical and Information Engineering
University of Oulu
Oulu, Finland

and

Professor Kai-Erik Peiponen
Department of Physics and Mathematics
University of Joensuu
Joensuu, Finland

ISBN 978-951-29-3911-4 (PRINT)
ISBN 978-951-29-3912-1 (PDF)
ISSN 0082-7002
Painosalama Oy – Turku, Finland 2009

Acknowledgements

The present work has been carried out in the Laboratory of Optics and Spectroscopy in the Department of Physics and Astronomy, University of Turku, during the years between 2004 and 2009.

I wish to express my sincerest gratitude to my supervisor, Professor Jyrki Kauppinen.

I am very gratefull to my co-authors Mr. Vesa Koskinen and Dr. Ismo Kauppinen.

The financial basis of this work was provided by the Graduate School of Modern Optics and Photonics, the Academy of Finland and Gasera Ltd.

I would also like to thank the members of the Laboratory of Optics and Spectroscopy for providing skillful technical and scientific support, and the personnel of the Laboratory of Optronics and Acoustics at the Defence Forces Technical Research Centre for their support and flexibility.

Prof. Kai-Erik Peiponen and Prof. Risto Myllylä are gratefully acknowledged for carefully reviewing this thesis. I owe my thanks to Dr. Milla Kibble for reviewing the English language of this thesis.

Abstract

A novel cantilever pressure sensor was developed in the Department of Physics at the University of Turku in order to solve the sensitivity problems which are encountered when condenser microphones are used in photoacoustic spectroscopy. The cantilever pressure sensor, combined with a laser interferometer for the measurement of the cantilever movements, proved to be highly sensitive. The original aim of this work was to integrate the sensor in a photoacoustic gas detector working in a differential measurement scheme. The integration was made successfully into three prototypes. In addition, the cantilever was also integrated in the photoacoustic FTIR measurement schemes of gas-, liquid-, and solid-phase samples. A theoretical model for the signal generation in each measurement scheme was created and the optimal cell design discussed.

The sensitivity and selectivity of the differential method were evaluated when a blackbody radiator and a mechanical chopper were used with CO_2, CH_4, CO, and C_2H_4 gases. The detection limits were in the sub-ppm level for all four gases with only a 1.3 second integration time and the cross interference was well below one percent for all gas combinations other than those between hydrocarbons. Sensitivity with other infrared sources was compared using ethylene as an example gas. In the comparison of sensitivity with different infrared sources the electrically modulated blackbody radiator gave a 35 times higher and the CO_2-laser a 100 times lower detection limit than the blackbody radiator with a mechanical chopper. As a conclusion, the differential system is well suited to rapid single gas measurements.

Gas-phase photoacoustic FTIR spectroscopy gives the best performance, when several components have to be analyzed simultaneously from multicomponent samples. Multicomponent measurements were demonstrated with a sample that contained different concentrations of CO_2, H_2O, CO, and four different hydrocarbons. It required an approximately 10 times longer measurement time to achieve the same detection limit for a single gas as with the differential system. The properties of the photoacoustic FTIR spectroscopy were also compared to conventional transmission FTIR spectroscopy by simulations.

Solid- and liquid-phase photoacoustic FTIR spectroscopy has several advantages compared to other techniques and therefore it also has a great variety of applications. A comparison of the signal-to-noise ratio between photoacoustic cells with a cantilever microphone and a condenser microphone was done with standard carbon black, polyethene, and sunflower oil samples. The cell with the cantilever microphone proved to have a 5-10 times higher signal-to-noise ratio than the reference detector, depending on the sample.

Cantilever enhanced photoacoustics will be an effective tool for gas detection and analysis of solid- and liquid-phase samples. The preliminary prototypes gave good results in all three measurement schemes that were studied. According to simulations, there are possibilities for further enhancement of the sensitivity, as well as other properties, of each system.

Preface

This thesis consists of the present introduction and the following publications (hereafter referred to as Papers [I] – [V]):

Paper [I] J. Kauppinen, V. Koskinen, J. Uotila and I. Kauppinen, "Extremely sensitive CWA analyzer based on a novel optical pressure sensor in photoacoustic gas analysis", in *Proc. of SPIE* **5617**, 115-127, 2004.

Paper [II] J. Uotila, V. Koskinen and J. Kauppinen, "Selective differential photoacoustic method for trace gas analysis", *Vibr. Spectrosc.* **38**, 3-9, 2005.

Paper [III] J. Uotila, "Comparison of infrared sources for a differential photoacoustic gas detection system", *Infrared Phys. & Tech.* **51**, 122-130, 2007.

Paper [IV] J. Uotila, "A new design of the differential photoacoustic gas detector combined with a cantilever microphone", *Eur. Phys. J. Special Topics* **153**, 401-404, 2008.

Paper [V] J. Uotila and J. Kauppinen, "Fourier transform infrared measurement of solid-, liquid-, and gas-phase samples with a single photoacoustic cell", *Appl. Spectrosc.* **62**, 655-660, 2008.

Chapter 1 is a short introduction to photoacoustic spectroscopy and provides the motivation for the thesis.

In Chapter 2 an optical cantilever microphone is introduced and its properties are discussed. The theory in this chapter is partly based on the theory presented in Paper [I], but mainly it is reformulated based on the new reference material.

Chapter 3 describes the use of the cantilever microphone in photoacoustic gas analysis. The focus is on the differential and FTIR methods. The discussion of the differential method is mainly based on Papers [II], [III], and [IV]. The signal generation with the cantilever microphone and optimization of the system are explained in more detail than in the articles.

Photoacoustic FTIR spectroscopy is discussed based on previously unpublished experiments and simulations. A detailed signal formation, discussion of spectral distortions and multicomponent measurements in photoacoustic FTIR spectroscopy, and optimization of the cell for FTIR spectroscopy are all presented for the first time in this thesis. Signal generation, calculation of the absorbance, and optimization of the cell length are briefly discussed also in Paper [V].

In Chapter 4, the properties and applicability of the cantilever microphone for the photoacoustic FTIR spectroscopy of solid- and liquid-phase samples are discussed. This chapter consists mainly of the study presented in Paper [V]. Signal generation is completed by incorporating the cantilever properties into the theory. The polyethene and sunflower oil spectra measured by the reference detector are added to the discussion about cell performance.

The conclusions of this work are drawn in Chapter 5.

Contents

Chapter 1

Introduction

Gas analyses have many applications in defense and security [1][2], atmospheric monitoring [3]-[5], industry [6], human health [7] and also in several other fields [8]. A considerable amount of commercial equipment is available, based on numerous different techniques [9]. However, several requirements still have not been fulfilled. There is always a need for more sensitive detectors. For some applications, only a small amount of the sample is available and extremely low sampling volumes are required. Often the gas has to be analyzed in ambient conditions and the number of false alarms has to be minimized. This means that the sensor has to be insensitive to cross interference from e.g. water vapor or hydrocarbons. The system should also be portable or handheld and it should be able to detect multiple gas components simultaneously.

Photoacoustics [10][11] is a promising technique which answers several of these requirements. The main limiting factor in photoacoustics has been the sensitivity of the condenser and electret microphones. The optical cantilever microphone offers a solution to this problem [12]. The combination of laser interferometer and micromachined silicon cantilever is allowing the measurement of pressure variations which are a hundred times lower than those detected by conventional microphones [13]-[16].

The principle of photoacoustic signal generation is rather simple. Electromagnetic radiation absorbed in a sample excites ground state molecules to the higher energy levels. The excited states relax either radiatively or non-radiatively. The non-radiative relaxations finally generate heat in a region of the infrared or light beam producing a pressure wave that propagates away from the source. A pressure sensor such as a microphone can be used to detect this acoustic wave. Periodically modulated light will generate an acoustic wave with a frequency equal to that of the modulation. In photoacoustics the absorption is measured directly, and the acoustic wave amplitude is proportional to the absorption and the concentration of the absorbing gas.

The measurement of solid-phase samples is well suited to photoacoustics and therefore it is included in the study. The FTIR (Fourier transform infrared) analysis of solid- and liquid-phase samples [17] has a great variety of applications [18] and advantages compared to other techniques. The most important and well-known advantages are the minimal sample preparation required, suitability for opaque materials, possibility for depth profiling, and nondestructive measurement, which means that the sample is not consumed. Photoacoustic spectroscopy is also suitable for powders, fibers and very small samples [19]. The shape of the photoacoustic spectrum is also independent of the morphology of the sample [20].

The photoacoustic phenomenon was invented as early as 1880 by Alexander Graham Bell, while experimenting with a photophone [21]. After this accidental discovery, several experiments with solid, liquid and gas samples were made [22]. However, the phenomenon remained in the background until the advent of the microphone. In 1938, Viengerov was able to evaluate gas concentrations using a blackbody radiator and an electrostatic microphone [23]. The first commercial photoacoustic gas analyzer was described by Luft [24] in 1943. He achieved major improvements in the sensitivity and selectivity by employing two photoacoustic cells in a differential design. At that time, photoacoustics was only used in gas analyses, and since gas chromatography performed better, photoacoustics played only a minor role. In the early 1970's the availability of lasers led to a major improvement in photoacoustics making it a very competitive and widely used method [25][26]. At the same time, interest in the solid-phase photoacoustics arose once again [27]-[29]. Nowadays solid-phase photoacoustic FTIR spectroscopy is a powerful tool for many applications [18]. A recent trend in photoacoustic gas analyses is to employ wavelength tunable quantum cascade and diode lasers [30][31].

The aim of this work has been to apply the optical cantilever microphone to photoacoustic spectroscopy (PAS), and to prove its potential and performance in selected practices of photoacoustics in gas analyses and also in FTIR spectroscopy of solid samples. Of the many techniques in the field of photoacoustic gas analysis, the differential and FTIR methods were chosen.

Chapter 2

Optical cantilever microphone

2.1. Cantilever and laser interferometer

A cantilever type pressure sensor has been proposed in order to achieve optimal sensitivity for a microphone used in a photoacoustic cell [12][13][15][16][32]. The main benefits of the cantilever are a very low string constant and extremely wide dynamical range in the cantilever movement. The string constant can be 2 or 3 orders of magnitude smaller than that of the membrane, and the movement of the cantilever can be tens of micrometers without any non-linear or restricting effects. An interferometric measurement of the cantilever end movement is required in order to avoid damping due to the probe and to maintain the wide dynamical range. The dynamics of the cantilever and condenser type microphones are discussed in Paper [I].

The cantilever is made out of silicon using a microfabrication process based on two-sided etching of silicon-on-insulator (SOI) wafers [33]. A thin cantilever moves like a saloon door induced by a pressure difference over the cantilever. The cantilever is typically 5 μm – 10 μm thick and it is supported by much thicker (300 μm – 500 μm) frames. On the three sides there is a narrow micrometer sized gap between the cantilever and its frame. The schematic drawing of the cantilever structure and typical dimensions are presented in Fig. 1.

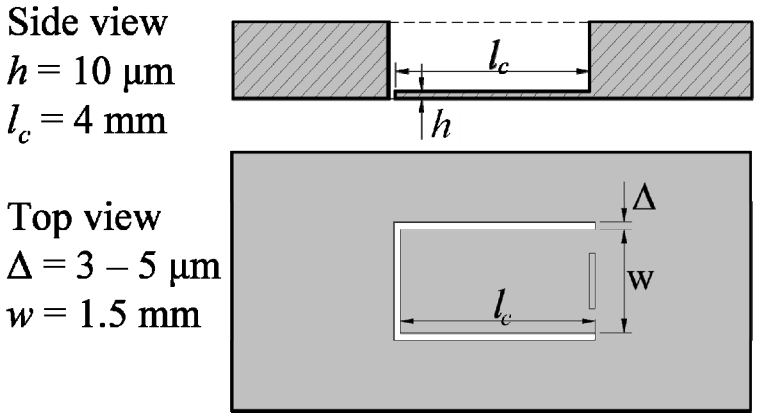

Figure 1. Cantilever structure and typical dimensions.

The optical measurement of the cantilever movement is based on a Michelson type laser interferometer (Fig. 2). The reference mirror in the interferometer is adjusted in such a way that only one interference fringe covers both photodiodes D1 and D2 having the phase difference of π/2. Respectively the photodiodes D3 and D4 in another branch have a phase difference of π/2. The signal in different branches automatically has a phase difference of π. The voltage signals U_1-U_4 and U_2-U_3 are calculated and subsequently the phase difference proportional to the cantilever displacement can be given as

$$\phi = \arctan\left(\frac{U_1 - U_4}{U_2 - U_3}\right). \tag{1}$$

If the phase difference exceeds 2π, the signal is calculated from the equation

$$s_n = \phi_n + 2\pi k_n, \text{ where } k_n = -\frac{\phi_n - 2s_{n-1} + s_{n-2}}{2\pi}. \tag{2}$$

Parameter k_n in Eq. (2) is rounded to the nearest integer. Unlike for the beam deflection technique [34], the dynamical range is extended because another interference fringe arises after the previous one disappears. The phase change of 2π corresponds to a displacement of λ/2 of the cantilever, where λ is the wavelength of the interferometer laser.

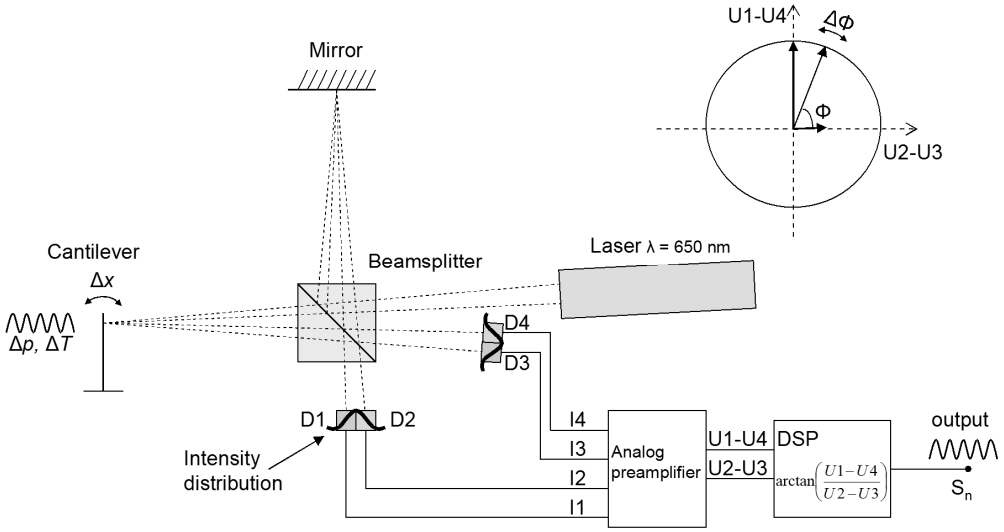

Figure 2. Schematic drawing of the laser interferometer and measurement principle.

2.2. Cantilever microphone versus condenser microphone

Condenser microphones are the most typical pressure sensors used in photoacoustic spectroscopy [35] and practically almost the sole type of microphones used in commercial devices. In a condenser microphone, the vibrating element is a flexible membrane. It deforms due to the pressure variations in the surrounding gas. In order to form a capacitor with the other electrode, the membrane has to be coated with metal. The capacitance C_M varies proportionally to the pressure Δp and the displacement of the membrane Δh_c as

$$\Delta C_M = -\frac{\varepsilon A_M}{h_c^2}\Delta h_c \propto \Delta p \qquad (\Delta h_c << h_c), \tag{3}$$

where ε is the dielectric constant of the gas between the electrodes, A_M is the common area of electrodes and h_c is the distance between electrodes. The sensitivity can be enhanced by increasing A_M and decreasing h_c. However, there is strong damping due to the air flow in and out of the gap between the electrodes that finally limits the sensitivity, when A_M is increased and h_c decreased enough. Optical measurement of the membrane displacement reduces damping. There are several techniques for optical measurement [36] e.g. optical beam deflection [34][37] and laser interferometry [38][39].

Significant improvements in microphone sensitivity can be achieved by using these methods. Also other pressure sensing methods such as flowmeters [40], a quartz tuning fork [41][42] and optical fibers [39][43] have been used successfully in photoacoustics.

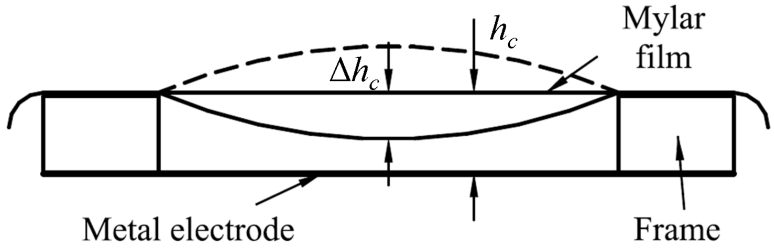

Figure 3. The structure of the condenser microphone.

When the flexible membrane is moving due to pressure variations it has to stretch. This causes additional damping and non-linearity to the pressure dependence of the membrane displacement. Instead of stretching, the cantilever bends. Therefore it is considerably more sensitive than the membrane to pressure variations. Below the first resonance frequency, the motion of the cantilever free end can be described using the simple one-dimensional point of mass model of a harmonic oscillator. The equation of motion is

$$m\ddot{x} + D\dot{x} + kx = F_{ext}(t), \tag{4}$$

where m is the effective mass, D is the damping constant, k is the effective string constant of the cantilever, $F_{ext}(t)$ is an external force, and t is time. The effective string constant depends on the cell and cantilever properties, but the string constant of the cantilever alone is

$$k_0 = \frac{2}{3} wY \left(\frac{h}{l_c} \right)^3, \tag{5}$$

where w is the width, l_c is the length, and h is the thickness of the cantilever, and Y is the Young's modulus of the material. When the external force is sinusoidal $F_{ext}(t) = F_0\cos(\omega t + \varphi)$, where F_0 is the amplitude of the force, ω is the angular frequency and φ is the phase difference, the amplitude of the displacement $x(t)$ in Eq.(4) can be solved. Then the frequency response or amplitude of the cantilever end displacement can be given as

$$A(\omega) = \sqrt{x^*(\omega)x(\omega)} = \frac{F_0}{m\sqrt{(\omega_0^2 - \omega^2)^2 + (\omega D/m)^2}}. \quad (6)$$

The resonance frequency is defined as $\omega_0 = \sqrt{k/m}$. Below the resonance frequency ($\omega << \omega_0$), the frequency response of the cantilever is constant $A(\omega) = F_0 / m\omega_0^2$, and above the resonance ($\omega >> \omega_0$) the response is inversely proportional to the square of the frequency $A(\omega) = F_0 / m\omega^2$. The cantilever has a major role in the total response, but there are also several other important mechanisms affecting the response of the signal in the photoacoustic cell (Fig. 4).

2.3. Cantilever in the photoacoustic cell

2.3.1. Photoacoustic cell response

There are various mechanisms acting in the photoacoustic system that affect the frequency response. In this chapter we discuss the generation of heat transfer, leakage and relaxation effects, which occur when the photoacoustic cell and cantilever pressure sensor are used for gas-phase measurements.

The photoacoustic cell dimensions are small compared to the wavelength of the excited acoustic wave. This allows us to assume that the pressure, temperature, and density of the gas are constant over the locations inside the cell. Therefore the equation of state of the ideal gas can be utilized

$$\frac{dp}{p} + \frac{dV}{V} = \frac{dT}{T}, \quad (7)$$

where p is the pressure, V is the volume, and T is the temperature of the gas in the cell. According to the first law of thermodynamics, the heat energy Q going into the ideal gas is

$$\delta Q = nc_V dT + pdV. \quad (8)$$

In Eq. (8), n is the number of moles and c_V is the specific heat capacity at constant volume. By substituting dT in Eq. (7) we have

$$\frac{dp}{p} + \gamma\frac{dV}{V} = \frac{(\gamma - 1)\delta Q}{pV}, \quad (9)$$

when the ratio of specific heat capacities is $\gamma = c_p/c_V$ and $c_p - c_V = R$, where R is the universal gas constant. The force affecting the cantilever due to a pressure change dp produces a displacement dx that depends on the cantilever string constant and area A_C as

$$k_0 dx = A_C dp \,. \tag{10}$$

The bending of the cantilever causes a small volume change in the photoacoustic cell. If this bending is assumed to be in the shape of an arc of a circle, the corresponding volume change is [15]

$$dV = \frac{2}{5} A_C dx \,. \tag{11}$$

A differential change in force can be obtained by substituting Eqs. (10) and (11) into Eq. (9)

$$dF = \left(k_0 + \gamma \frac{A_C^2 p}{2.5V} \right) dx = \frac{A_C (\gamma - 1) \delta Q}{V} \,. \tag{12}$$

An effective string constant k of the cantilever inside the photoacoustic cell can be deduced from the left side of the equation. The volume change due to the bending is added to the cantilever string constant leading to the effective value of

$$k = k_0 + \gamma \frac{A_C^2 p}{2.5 V_{eff}} \,. \tag{13}$$

If the volume at the rear of the cantilever, V_0, is small, the sample cell volume V in Eq. (12) has to be replaced with an effective volume V_{eff} determined as

$$\frac{1}{V_{eff}} = \frac{1}{V} + \frac{1}{V_0} \,. \tag{14}$$

By integrating the latter part of Eq. (12), which describes the force on the cantilever due to the external heating energy, we can write the external harmonic force as

$$F_{ext}(t) = \frac{A_C (\gamma - 1)}{V} \int \frac{\delta Q}{dt} dt \,. \tag{15}$$

The heating of a sample gas is induced by the absorption of energy from modulated infrared radiation, as stated by Beer's absorption law. We can assume that the thermal conduction of the cell walls is high compared to thermal conduction through the gas, that the heat capacity of the cell walls is high compared to that of the gas, and the energy transfer to heat is isochoric, $\delta Q = C_V dT$, where C_V is the total heat capacity of the gas in the sample cell. Under these assumptions a solution to the integral in Eq. (15) can be found [15]:

$$\int \frac{dQ}{dt} dt = \frac{\left[1 - \exp(-\alpha_x l)\right] P_0 \dfrac{C_V}{G}}{\sqrt{1 + \left(\dfrac{C_V}{G}\omega\right)^2}} \cos(\omega t + \varphi'), \tag{16}$$

where α_x is the absorption coefficient of the absorbing gas, l is the absorption length, P_0 is the maximum power of the infrared radiation, G is the total thermal conductivity of gas content inside the cell, and φ' is the phase shift. Now we can substitute Eq. (16) into Eq. (15) and substitute the external force into the equation of motion and construct the frequency response which includes the heating effect as

$$A(\omega) = \frac{A_C(\gamma - 1)}{V} \frac{\left[1 - \exp(-\alpha_x l)\right] P_0}{m\sqrt{(\omega_0^2 - \omega^2)^2 + (\omega D/m)^2}} \frac{\tau_1}{\sqrt{1 + (\omega\tau_1)^2}}, \tag{17}$$

where the time constant $\tau_1 = C_V / G$. A good approximation to the time constant due to gas heating can be given by [15]

$$\tau_1 \approx \frac{\rho c_v r^2}{5.78K}, \tag{18}$$

when a long cylindrical cell is used and homogenous heat energy absorption along the cell is assumed. In the Eq. (18) ρ is the density, c_v is the specific heat capacity (constant volume), K is the thermal conductivity of the gas, and r is the radius of the cell.

Thermal diffusion to the cell walls prevents the absorbed energy near the cell surface from forming a photoacoustic signal, instead the heat is conducted to the cell walls. The thermal diffusion length, μ, describes the distance where 37 % (1/*e*) of the heat is conducted to the wall and can be given as

$$\mu = \sqrt{\frac{2K}{\omega \rho c_p}}, \tag{19}$$

where c_p is the specific heat capacity (constant pressure) of the gas mixture in the cell. The effect of this thermal diffusion on the photoacoustic signal can be approximated by multiplying the signal by the factor

$$W(r) = 1 - \frac{\mu}{r}\left[1 - \exp\left(-\frac{2r}{\mu}\right)\right]. \tag{20}$$

By *leakage* through the gap between the cantilever and the frame, we mean both the direct leaking of gas through the gap, which is damping the pressure difference, and also the effect on the temperature variation in the sample cell, due to the energy transfer away from the sample cell by higher temperature gas molecules. Both mechanisms act as highpass filters in the system giving a frequency response of

$$A_{23}(\omega) = A(\omega)\frac{\omega\tau_{23}}{\sqrt{1+(\omega\tau_{23})^2}}. \tag{21}$$

The combined effect due to pressure and temperature differences can be regarded as a serial process, and an approximation to the effective time constant τ_{23} is given by [15]

$$\frac{1}{\tau_{23}} = \frac{1}{\tau_2} + \frac{1}{\tau_3} = \frac{A_g}{2V_{eff}}v_{rms} + \frac{A_g}{4\sqrt{3}V_{eff}}v_{rms} = \frac{3A_g}{4\sqrt{\gamma}V_{eff}}v_{sound}, \tag{22}$$

where τ_2 is the time constant due to the pressure difference, τ_3 is the time constant due to the temperature difference, A_g is the area of the gap between the cantilever and its frame, v_{rms} is the root-mean-square of the molecule velocities in the photoacoustic cell and v_{sound} is the speed of sound.

Relaxation mechanisms of excited molecules to heat via a non-radiative pathway might be complicated. The relaxation time depends on the pathway and excited energy levels [10]. The total effect of relaxation process can be described by a lowpass filter using one relaxation time τ_4, which is typically less than 1 millisecond. The frequency response of the process is [15]

$$A_4(\omega) = \frac{A(\omega)}{\sqrt{1+(\omega\tau_4)^2}}. \tag{23}$$

The resonance frequency of the cantilever inside the photoacoustic cell depends on the effective mass and the string constant: $\omega_0 = \sqrt{k/m}$. The effective string constant is given in Eq. (13). The effective mass is given by summing the oscillating portion of the cantilever mass and the mass of the moving gas which the cantilever displacement is pushing through the cell parts. It can be easily determined by measuring the resonance frequency, but we can only give an analytical form as an approximation [15]:

$$m \approx \frac{2}{3}m_C + \rho_{gas}\sum_{i,j}\frac{(0.4A_C)^2}{V_{j,tot}^2 A_{i,j}}\left[\frac{V_{i,j}^2}{3} + V_{i,j}V_{i,j,end} + V_{i,j,end}^2\right]l_{i,j}, \tag{24}$$

where m_C is the mass and A_C is the area of the cantilever, and ρ_{gas} is the density of the gas in the cell. $V_{j,tot}$ is the total volume in side j of cantilever, $A_{i,j}$ is the area, $l_{i,j}$ is the length, $V_{i,j}$ is the volume of the chamber before, and $V_{i,j,end}$ is the volume after the channel i, where the gas is forced to move due to the cantilever displacement.

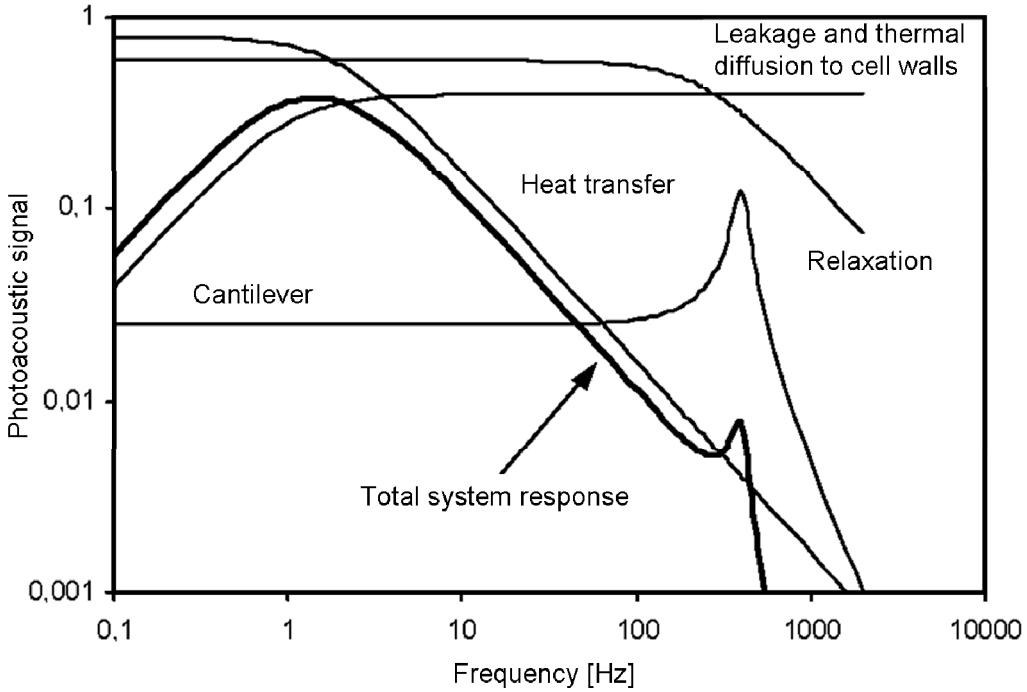

Figure 4. The impact of each component on the photoacoustic cell response.

The total system response which combines the effects of the cantilever, gas heating, leakage through the gap and relaxation of excited molecules, is

$$A(\omega) = \frac{A_C(\gamma - 1)}{V} \frac{\left[1 - \exp(-\alpha_x l)\right] P_0}{m\sqrt{(\omega_0^2 - \omega^2)^2 + (\omega D / m)^2}} \\ W(r,\omega) \frac{\tau_1}{\sqrt{1 + (\omega\tau_1)^2}} \frac{\omega\tau_{23}}{\sqrt{1 + (\omega\tau_{23})^2}} \frac{1}{\sqrt{1 + (\omega\tau_4)^2}} . \quad (25)$$

In Fig. 4 the response of each component is shown separately. The response of the cantilever is constant until the resonance frequency. At low frequencies heat transfer and leakage effects dominate the shape of the response giving a maximum of the total system at the frequency range between 1 Hz and 10 Hz. After the resonance frequency the response decreases rapidly limiting the feasible measurement range below the resonance frequency.

2.3.2. Noise sources

The sensitivity of the gas detection system is ultimately limited by the signal-to-noise ratio (SNR). Therefore it is not enough just to have a high response, the noise characteristics of the system must also be known. A photoacoustic cantilever system basically has four kinds of noise: acceleration, acoustic, electrical, and Brownian noise. Also a high background signal can increase noise due to the instability of the infrared radiation source.

Acceleration noise is generated by the movement of the instrument which disturbs the cantilever. The most disturbing is acceleration perpendicular to the cantilever surface that makes the cantilever bend because of inertia. The acceleration noise in this direction is minimized by a balance structure of the cells (Fig. 5). The principle is to let the acceleration induce a pressure difference between the cantilever sides in such a way that a compensating force on the cantilever is induced. This is done by positioning the centers of mass of the sample and balance chambers at the same side of the cantilever at an appropriate distance. A simple equation for the optimal distance d_{CM} can be calculated as follows: [15][16]

$$d_{CM} = \frac{\rho_{cant}}{\rho_{gas}} h , \quad (26)$$

where ρ_{cant} is the density of the cantilever, ρ_{gas} is the density of the gas in the cell, and h is the thickness of the cantilever. The acceleration noise can also be significantly reduced by using mechanical vibration dampers, e.g. gel pads, or a two cantilever system, where acceleration bends the cantilevers in the same direction and the signal in opposite directions. By calculating the sum-signal acceleration noise is subtracted. Typically, acceleration noise can be damped at high frequencies, but at frequencies below 25 Hz it is dominating.

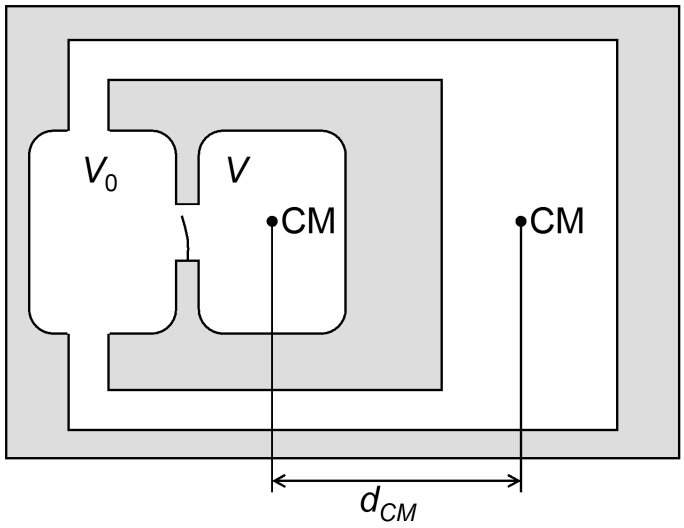

Figure 5. Acceleration noise can be damped by adjusting the distance between the centre of mass of the sample and balance chambers.

Acoustic noise is generated from ambient sound that makes weak structures in the system vibrate or enters the photoacoustic cell through small holes in the construction. Usually the appearance of acoustic noise is a sign of failure in the system construction and normal ambient noise is attenuated when a proper design and materials are used.

Electrical noise is formed in the analog electronics, photodiodes and AD-converters of the system. Also laser intensity fluctuations in the optical read out system create electrical noise. All of these noise sources have different frequency characteristics. In a typical cantilever based photoacoustic system, the electrical noise is much lower than other noise sources except at the modulation frequency of the power network (50 Hz or 60 Hz).

Brownian noise is the ultimate limiting factor, when external noise sources are damped. Thermal fluctuations generate a random force on the cantilever. The cantilever senses fluctuations through collisions of the molecules in the gas

medium. The frequency characteristics of the Brownian noise can be evaluated by dividing the noise into the 1/*f*-component and the oscillating component, and normalizing the power spectrum with the expectation value of the potential energy as [15]

$$\frac{1}{2}k\left\langle x^2(t)\right\rangle = \frac{1}{2}k_B T\,. \tag{27}$$

The gap between the cantilever and its frame generates the 1/*f*-component [44], which is an additional part to the oscillating component considered in the traditional treatment of the Brownian motion of cantilevers [45]. The normalization leads to a situation where the increase in the Q-value decreases the noise elsewhere, especially at low frequencies. The power spectrum of the Brownian noise follows the signal spectrum close to the resonance, but at low frequencies the cantilever dimensions can significantly affect the signal-to-noise ratio. Typically the signal-to-noise ratio has a maximum value at frequencies between 10 Hz – 50 Hz. In Fig. 6 the measured noise spectrum dominated by Brownian noise is presented.

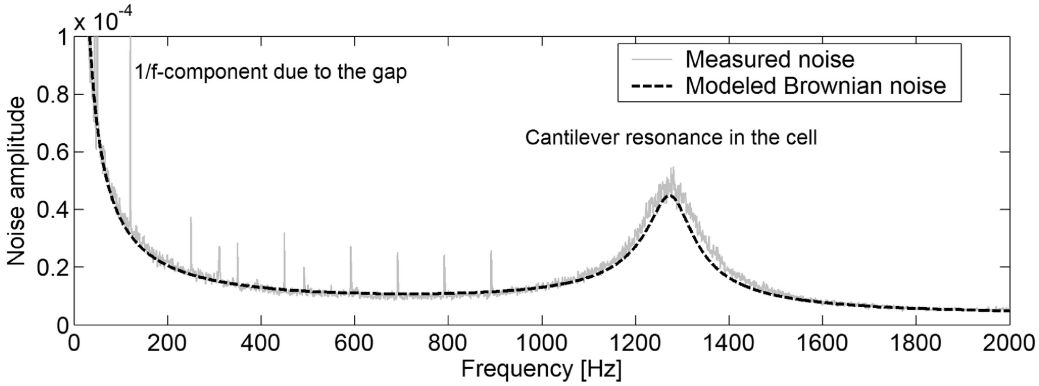

Figure 6. Measured noise spectrum, where Brownian noise is dominating.

A background signal is generated in the photoacoustic cell walls, cell windows, and dust in the cell. If the background signal is high, the intensity variations in the radiation source create noise even if the signal itself can be subtracted. The wall signal is minimized by polishing and gold coating the cell walls making them highly reflective. The window signal is generated by the absorption of infrared radiation into the window material and the temperature fluctuation on the gas close to the window surface forming an acoustic signal. A dust signal is generated by small particles in the photoacoustic cell that absorb infrared radiation. A dust filter can be used in the gas inlet in order to prevent any particles getting into the cell. Wall and window signals can also be minimized by using a differential setup or a frequency modulation with laser sources.

Chapter 3

Photoacoustic spectroscopy of gas-phase samples

3.1. Measurement techniques

There are basically four different techniques that have been used for photoacoustic detection of gas-phase samples: systems with laser sources, systems with a blackbody radiator and optical filters, differential systems, and FTIR systems. Each of these techniques has benefits and drawbacks, which dictate the suitable applications for which they should be used. The key issue that each approaches differently is selectivity. There are also other important properties that vary for the different setups such as sensitivity, linearity, sampling, complexity, and system cost. An optical cantilever microphone can be integrated in any of the four setups. Possible infrared sources that can be used with photoacoustics, other than those mentioned above, are for example LEDs [46] and super continuum lasers [47].

Laser sources are currently the most frequently applied infrared sources in photoacoustics [1][6][8]. Usually they are used in combination with a resonant photoacoustic cell [48]. In the past gas lasers have been the most practical mid-infrared lasers, having high power in fundamental vibrational bands of several interesting gas species [3]. Recently the development of semiconductor diode lasers and quantum cascade lasers has made laser sources available in greater variety of wavelengths, also on the bands of fundamental transitions [8][49]. With diode lasers high power levels can be reached by using fiber amplifiers [50][51], but the greatest advantage is their tunability. Selectivity with lasers is based on the narrow laser linewidth. It can be tuned precisely to the gas absorption line that gives the highest signal for a specific gas species completely without, or with only minor, cross interferences. Wavelength

modulation of diode lasers minimizes the background signal and avoids vibrations due to the mechanical chopper. The photoacoustic cell with a cantilever pressure sensor is a simple cylinder working in non-resonant mode, when a laser source is used. Good results have been achieved in several studies by combining the diode laser and cantilever system, where a cantilever based cell is compared to other photoacoustic cells [13][51]-[55]. At best, a normalized noise equivalent sensitivity (NNEA) of $1.7 \cdot 10^{-10}$ cm^{-1} W $Hz^{-1/2}$ has been reported [52], being ca. 100 times better than with condenser microphones [50] and more than 10 times better than with a quartz tuning fork [41].

The blackbody radiator and optical filters are also used in commercial photoacoustic gas analyzers [56]. Selectivity is achieved by selecting infrared pass bands of the filters according to the gas to be measured. Cross interference is much higher than with lasers due to the wider pass band of the filter. However, by using several filters many substances can be separated sufficiently well. Large size high temperature blackbody sources create a high signal, when fundamental vibrational bands are excited. The radiation cannot be both collected on a wide space angle and focused on a small area at the same time and also a mechanical chopper has to be used with large sources. Another possibility is to use electrically modulated blackbody sources [57][58]. By using these sources, system becomes more rugged, simpler and also lower cost, but sensitivity is decreased. When the cantilever enhanced photoacoustic cell is designed for blackbody sources, the cell is cylinder shaped, but the diameter is larger than in the design for laser sources.

3.2. Differential setup

The differential system was the first photoacoustic technique to be used in a commercial gas analyzer [24]. Its benefits, compared to systems with direct absorption measurement, are the subtraction of background signals due to the cell walls and windows, a high selectivity due to the gas spectrum acting as a filter, and immunity of the photoacoustic cell to noise while the sample is changed. This means that no additional filters are required, for example when CO_2 is measured, noise due to the short term instability of the light source is canceled, and the sample cell can be completely open or the gas can flow continuously during the measurement. The sampling interval can be very short when using a differential cell. The devices in literature based on differential photoacoustic systems are usually called NDIR (nondispersive infrared spectroscopy) gas analyzers [59]-[63]. There are also systems called "differential mode excitation photoacoustic spectroscopy" (DME-PAS) detectors that use a reference signal from another frequency in order to

compensate for instability due to intensity fluctuations of the light source or drifts in the microphone response and electronics [64][46].

3.2.1. Signal generation in differential method

Selectivity in the differential method is based on gas filter correlation (GFC) [65]-[67]. When gas filter correlation is applied with a cantilever microphone, the system consists of three cells: the sample cell, reference cell, and photoacoustic cell (Fig. 7). The sample cell contains the unknown sample gas which includes component whose concentration is determined and possibly some other components. The reference cell contains a non-absorbing gas, such as nitrogen. The photoacoustic cell acts as a selective detector and contains a high amount of the gas to be detected. It is divided in two similar parts A and B, which are separated by the cantilever. The displacement of the cantilever depends on the pressure difference between cell parts A and B.

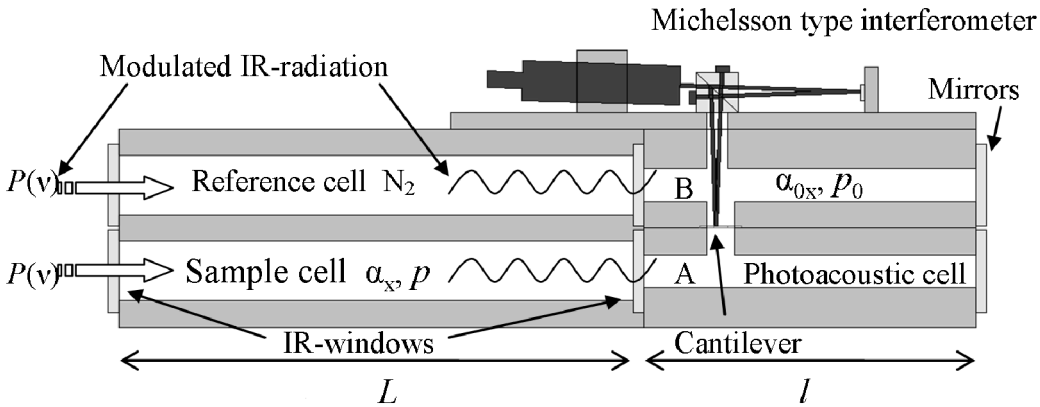

Figure 7. Schematic drawing of the differential setup.

The amplitude of the cantilever displacement due to the photoacoustic signal in cell part A is

$$A = C(\omega) \times \int_0^\infty P(\nu) \exp(-\alpha_x(\nu) L) \left[1 - \exp(-\alpha_{0x}(\nu) l)\right] \mathrm{d}\nu \,, \tag{28}$$

where $P(\nu)$ is the radiation power coming into the sample cell, α_x is the absorption coefficient of gas component x in the sample cell, L is the absorption length in the sample cell, α_{0x} is the absorption coefficient of gas component x in the photoacoustic cell, l is the absorption length in the photoacoustic cell, and ν

is the wavenumber. The cell constant $C(\omega)$, which describes the response of the photoacoustic cell, can be derived from Eq. (25) as

$$C(\omega) = \frac{A_C(\gamma-1)W(r,\omega)}{V\sqrt{(k-m\omega^2)^2+(\omega D)^2}} \frac{\tau_1}{\sqrt{1+(\omega\tau_1)^2}} \frac{\omega\tau_{23}}{\sqrt{1+(\omega\tau_{23})^2}} \frac{1}{\sqrt{1+(\omega\tau_4)^2}}. \quad (29)$$

Respectively the amplitude in cell part B is

$$B = C(\omega) \times \int_0^\infty [1-\exp(-\alpha_{0x}(\nu)l)]P(\nu)\mathrm{d}\nu. \quad (30)$$

Furthermore the difference signal can be calculated from Eqs. (28) and (30) as

$$B - A = C(\omega) \times \int_0^\infty P(\nu)[1-\exp(-\alpha_x(\nu)L)][1-\exp(-\alpha_{0x}(\nu)l)]\mathrm{d}\nu. \quad (31)$$

The absorption coefficient, $\alpha_x(\nu)$, is a sum of effective absorption coefficients of individual transitions between states η and η'

$$\alpha_x(\nu) = \sum \overline{\alpha}_{\eta\eta'}(\nu) \equiv p_x E_x(\nu), \quad (32)$$

where $E_x(\nu)$ is the absorption spectrum of component x. An effective absorption coefficient can be written as [68]

$$\overline{\alpha}_{\eta\eta'}(\nu) = S_{\eta\eta'}(T)\frac{p_x}{kT}\frac{10^{-6}}{1.013}g(\nu), \quad (33)$$

when the partial pressure p_x of gas component x is expressed in units of [atm] and $S_{\eta\eta'}$ is the line intensity. The normalized line shape function $g(\nu)$ describes the spectral line spread about the transition frequency. When absorption in the sample cell is small, the difference signal is linearly proportional to the partial pressure

$$B - A \approx p_x \cdot C(\omega)\int_0^\infty P(\nu)[1-\exp(-\alpha_{0x}(\nu)l)]E_x(\nu)L\,\mathrm{d}\nu. \quad (34)$$

Under atmospheric conditions, pressure broadening dominates the spectral linewidth. The pressure broadening varies according to whether it is

caused by collisions of molecules of the gas compound itself or molecules of some other compounds. The resulting linewidth (HWHM) is given by [68]

$$\Delta\nu^{p}_{\eta\eta'} = \left(2\gamma^{air}_{\eta\eta'}(p - p_x) + 2\gamma^{x}_{\eta\eta'}p_x\right)\cdot\left(\frac{T}{T_{ref}}\right)^{-n_{\eta\eta'}}, \tag{35}$$

where $\gamma^{air}_{\eta\eta'}$ and $\gamma^{x}_{\eta\eta'}$ are the air broadened and self-broadened halfwidth at half maximum at reference temperature T_{ref} = 296 K and pressure 1 atm, and $n_{\eta\eta'}$ is the coefficient of temperature dependence. Pressure broadening can be approximated well using the line shape function of the Lorenz profile [68]

$$g(\nu) = \frac{\Delta\nu^{p}_{\eta\eta'}/2\pi}{(\nu - \nu^{p}_{\eta\eta'})^2 + (\Delta\nu^{p}_{\eta\eta'}/2)^2}. \tag{36}$$

At low pressures, high wavenumbers, and high temperatures Doppler broadening becomes significant. The Doppler linewidth is

$$\Delta\nu_D = \nu_{\eta\eta'}\sqrt{\frac{2kT}{mc^2}\ln 2}, \tag{37}$$

where m is the molecular mass and c is the speed of light. The line shape function due to the Doppler broadening is [68]

$$g_D(\nu) = \frac{1}{\nu_{\eta\eta'}}\sqrt{\frac{mc^2}{2\pi kT}}\exp\left(-\frac{mc^2}{2kT}\frac{(\nu - \nu_{\eta\eta'})^2}{\nu^2_{\eta\eta'}}\right). \tag{38}$$

When pressure broadening is comparable to Doppler broadening, the Voigt absorption profile is calculated as a convolution of the two line shape functions. A simulation of the absorptance spectra $A_x(\nu) = 1 - \exp(-\alpha_x(\nu)L)$ and $A_{0x}(\nu) = 1 - \exp(-\alpha_{0x}(\nu)l)$ of 100 ppm of carbon dioxide in the sample cell and 5000 ppm of carbon dioxide in the photoacoustic cell are shown in Fig. 8. The line shape function is approximated using the Lorenz profile and the absorption length is set to 14.9 cm in the sample cell and to 7 cm in the photoacoustic cell.

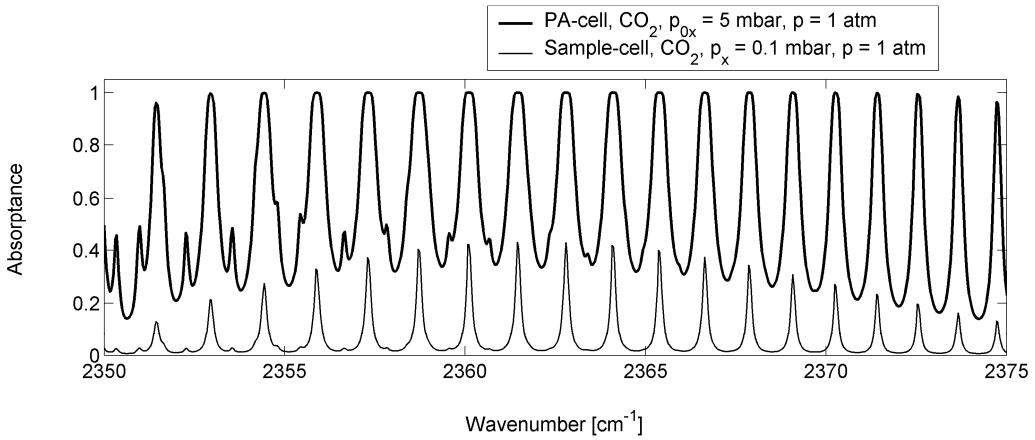

Figure 8. Simulated absorptance spectra of carbon dioxide in the sample and photoacoustic cells.

3.2.2. Selectivity

The absorption spectrum of the gas inside the photoacoustic cell provides the selectivity. When absorption coefficients of components x and y are α_x and α_y, and photoacoustic cell is filled with component x with absorption coefficient α_{0x}, the amplitude A can be given by

$$A = C(\omega)\int_0^\infty P(\nu)\cdot\exp(-\alpha_x(\nu)L)\cdot\exp(-\alpha_y(\nu)L)\cdot\left[1-\exp(-\alpha_{0x}(\nu)l)\right]\mathrm{d}\nu\,. \tag{39}$$

If absorbances $p_xE_x(\nu)L \ll 1$ and $p_yE_y(\nu)L \ll 1$ are small, the difference signal is

$$B - A = C(\omega)p_xL\int_0^\infty P(\nu)E_x(\nu)A_{0x}(\nu)\mathrm{d}\nu + C(\omega)p_yL\int_0^\infty P(\nu)E_y(\nu)A_{0x}(\nu)\mathrm{d}\nu\,, \tag{40}$$

where the absorptance of the gas in the photoacoustic cell is given by $A_{0x} = 1 - \exp(-\alpha_{0x}(\nu)l)$. When Eqs. (34) and (40) are compared, it can be seen that the two-component sample gives a signal that is a sum of a single substance signal and a cross interference signal. The cross interference depends on the partial pressure of the cross interfering substance and the cross correlation of the absorption spectrum of interfering substance and the absorptance spectrum of the gas in the photoacoustic cell. This result can be generalized for multicomponent samples as

$$B - A = C(\omega) p_x L \int_0^\infty P(\nu) E_x(\nu) A_{0x}(\nu) \mathrm{d}\nu + C(\omega) \sum_i p_i L \int_0^\infty P(\nu) E_i(\nu) A_{0x}(\nu) \mathrm{d}\nu \,. \quad (41)$$

The cross correlation can be minimized by using a low total pressure and partial pressures in the photoacoustic cell, and if necessary, using additional optical filters which affect the band of input power $P(\nu)$.

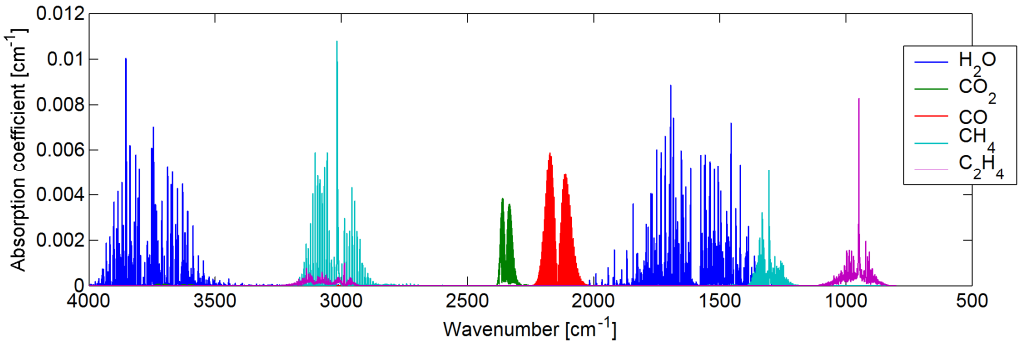

Figure 9. Simulated absorption coefficient spectra of H_2O (300 ppm), CO_2 (10 ppm), CO (100 ppm), CH_4 (100 ppm) and C_2H_4 (100 ppm).

The selectivity of the system for a pair of components can be described using the cross sensitivity Q_{xy}, which is determined as a ratio of the single substance signal and the cross interference signal [69]

$$Q_{xy} = \frac{(B - A)_{xy}}{(B - A)_{xx}} \,. \quad (42)$$

In fact, the signals are the second and first term on the right hand side of the Eq. (40). In Table I, the cross sensitivities are calculated for five example gases using dimensions L = 14.7 cm and l = 19.0 cm, and a partial pressure p_{0x} = 100 mbar. Also measured detection limits for each gas are shown. The absorption coefficient spectra of these five components are shown in Fig. 9. The simulation and measurement results are created according to experiments presented in Paper [III].

Table I. Simulated cross sensitivities and measured detection limits of H_2O, CO_2, CO, CH_4 and C_2H_4 for a 1.3 s measurement time.

Comp. y in the sample cell	Component x in the photoacoustic cell				
	C_2H_4	CH_4	CO_2	CO	Det. limit / ppm
C_2H_4	1	1.2×10^{-1}	4.6×10^{-5}	1.6×10^{-5}	0.92
CH_4	6.3×10^{-1}	1	1.8×10^{-5}	7.7×10^{-4}	0.32
CO_2	1.9×10^{-4}	2.7×10^{-3}	1	3.1×10^{-4}	0.11
CO	3.0×10^{-5}	5.3×10^{-4}	1.7×10^{-4}	1	0.80
H_2O	2.3×10^{-3}	1.2×10^{-2}	1.4×10^{-2}	2.4×10^{-4}	

Good selectivity can be achieved, when dissimilar components e.g. CO_2 and CH_4 are separated, but, for example, between hydrocarbons the selectivity is insufficient if there are several substances in the sample. Depending on the application, an additional narrowing of the spectral band may be required.

3.2.3. Optimization of the differential system parameters

Optimizing the system parameters for the best possible sensitivity means finding the highest possible signal-to-noise ratio induced by the partial pressure p_x of the sample gas. In order to do this, the cell constant, incoming optical power, absorptance in the sample cell and absorptance in the photoacoustic cell all have to be as high as possible (Eq. 31), whilst the noise is minimized. These parameters can be adjusted through the selection of the infrared source, cantilever and cell dimensions, pressure in the cells, and the mixture in the photoacoustic cell. The optimization is complicated in the sense that each selection affects the others and parameters cannot be optimized separately. However, there are certain principles that can be used for optimization.

The partial pressure of the gas to be detected in the photoacoustic cell should be high enough to absorb nearly 100 percent of the radiation at relevant wavelengths, even when the sample cell length is short. The photoacoustic cell length should be chosen to optimize the volume of the cell to ensure the highest possible cell constant, whereas the cell diameter having been determined by the optical beam geometry. The cell constant Eq. (29) is effectively determined by the volume of the gas to be heated, the leakage through the frame gap Eqs. (21) and (22), and the gas string constant Eq. (13) interacting with the cantilever, which all depend on the volume of the cell. The cantilever dimensions have a direct effect on the signal, but also on the optimal volume of the cell. Generally the cantilever should be as thin and long as

manufacturing allows, and the frame gap should be as small as possible. The smaller the cantilever dimensions, the lower the optimal volume and the higher the signal. This is demonstrated in Fig. 10, where the signal amplitude at 40 Hz is calculated for four cantilevers of different sizes. A cylinder shaped cell is assumed with a diameter of 3 mm.

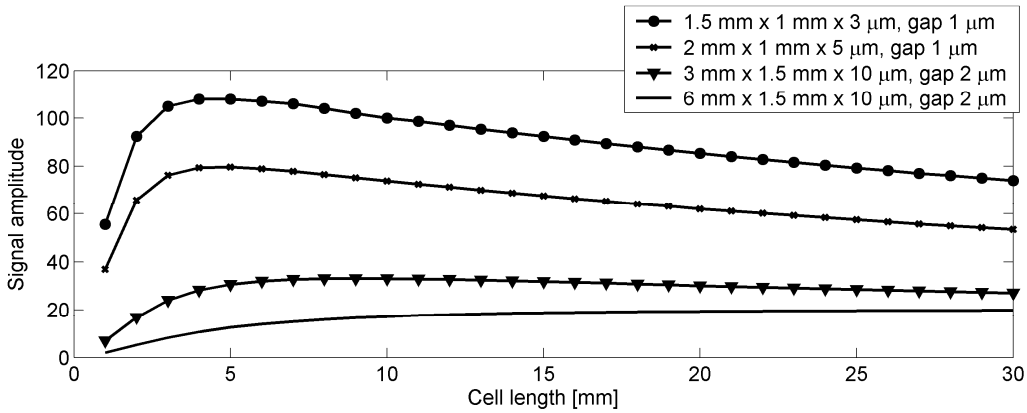

Figure 10. Simulated signal amplitude as a function of the photoacoustic cell length with four different cantilevers.

Not only the partial pressure of the gas to be detected, but also the total pressure and the properties of the mixing gas influence the signal. The gas string constant, moving mass and damping constant depend on the pressure, the leakage time constant depends on the sound velocity, and ratio of specific heat capacities on the mixture substances. The use of lower pressures increases the signal to a point where the decrease of absorption starts to dominate. In Fig. 11 the detection limit for methane is measured by setting the mixture of methane and argon (CH_4 10 %, Ar 90 %) in the photoacoustic cell at different pressures. In this case the highest sensitivity is reached at 130 mbar. A more detailed description of the experiments is presented in Paper [II].

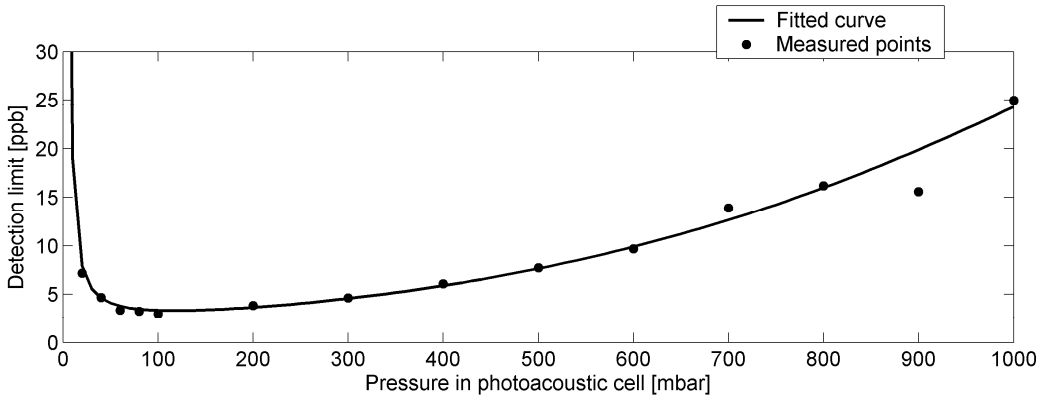

Figure 11. Measured detection limits for methane at different photoacoustic cell pressures. The photoacoustic cell contained a mixture of methane (10 %) and argon (90 %) at different pressures. The sample cell length was ca. 100 cm.

The modulation frequency usually has an optimal value at frequencies well below 100 Hz. At the frequencies below 20 Hz, the noise due to external vibrations might dominate, but at higher frequencies the dominating noise is due to the Brownian motion of gas molecules. In Fig. 12 the signal-to-noise ratio is presented as a function of frequency in a case where the cantilever dimensions are: 2 mm x 1 mm x 5 μm, gap 1 μm, and the cell dimensions are: diameter 3 mm, length 10 mm. The maximum of the signal-to-noise ratio in the figure is approximately at 70 Hz.

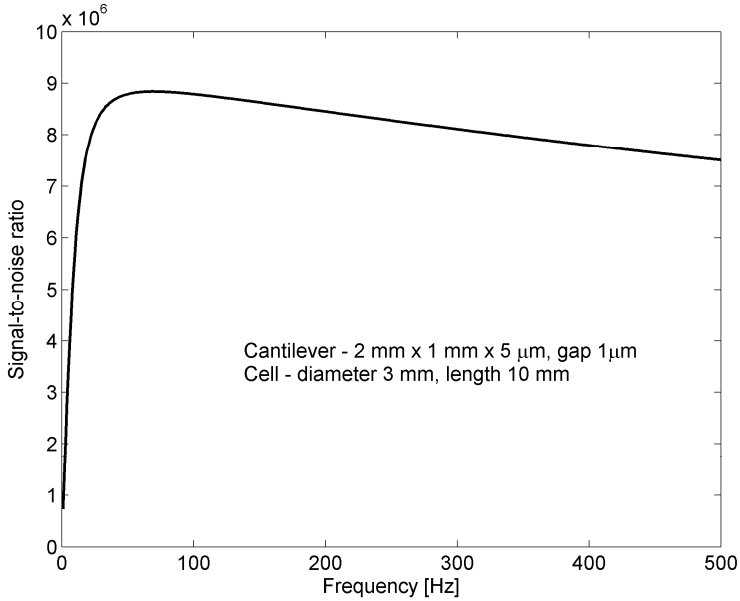

Figure 12. Simulated signal-to-noise ratio when Brownian noise is assumed to be the dominating noise source.

The sample gas mixture or pressure are usually determined by the application. If there are no cross interferences and the sample concentration is very low, it is advantageous to use as long a sample cell as practically possible in order to achieve the highest sensitivity. Some applications of the differential system require determining small variations in a high concentration. In this case the reference cell can also be filled with the high concentration of gas to be detected in order to adjust the difference signal to zero at this specific concentration. Therefore the sample cell length cannot be long, otherwise too much radiation would be absorbed without causing the signal. The optimal sample cell length is achieved, when the condition $\alpha_x L = 1$ is fulfilled. An example of the variation in transmittance as a function of the cell length, when the concentration is altered by 1 ppm, is shown in Fig. 13. The absorption coefficient from the water absorption line at 2.67 μm is used in the calculation. The total concentration of the water vapor has a strong influence on the signal.

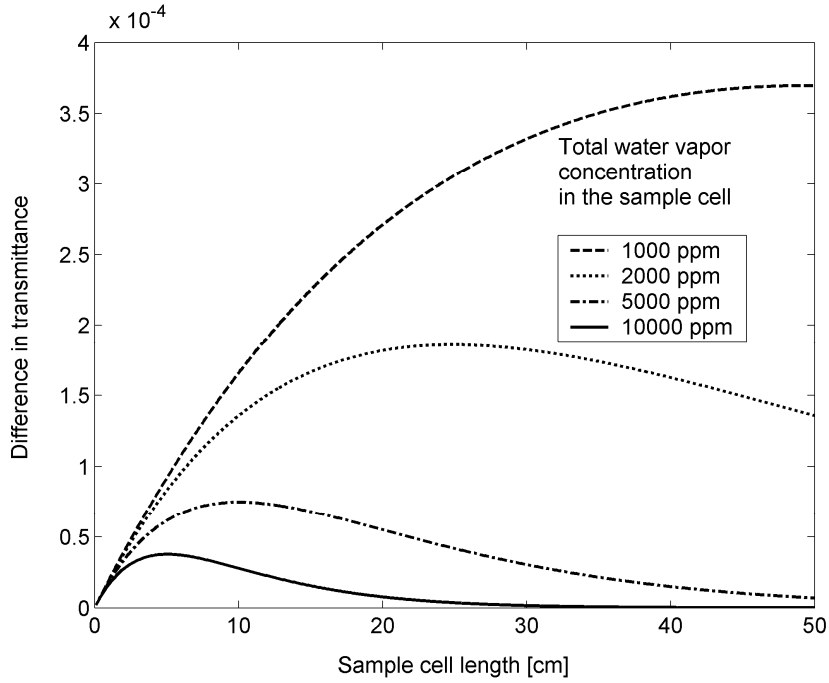

Figure 13. Variation of transmittance in the sample cell with different water vapor concentrations and sample cell lengths, when the water concentration is altered by 1 ppm.

3.2.4. Selection of the infrared source

Large blackbody radiators are well suited to the differential setup, because they give a relatively high energy density on the fundamental vibrational bands, exciting all transitions simultaneously. Selectivity is provided by the gas filter correlation and possibly additional optical filters. The mechanical chopper generates external vibrations at the chopping frequency and tuning the signal to the zero level with shutters is challenging, because of the phase differences between the two sides of the detector which is due to the large size and the geometry of the beam. The use of electrically modulated blackbody radiators removes the vibrations due to the chopper and eases the zero level tuning. The signal with these sources is low, since their area is very small. These sources also have a relatively low temperature, and the modulation depth decreases rapidly when the frequency is increased. If the selectivity or sensitivity is not sufficient, laser sources can be used. Selectivity with lasers does not require the differential setup, but sampling in some applications might. Zero level tuning with lasers can be done by using the neutral density filter or polarizer in order to avoid geometrical effects which cause phase differences. The modulation technique depends on the laser type, but the frequency can usually be freely selected.

Three experimental setups (Fig. 14) were used to compare the sensitivity for a large mechanically chopped blackbody radiator, an electrically modulated blackbody radiator and a CO_2-laser. The first setup was built using a large blackbody radiator (5 mm in diameter) with a focusing mirror and mechanical chopper. The pressure signal in the photoacoustic cell parts was set in the same phase by chopping the beam on the focal point of the elliptic mirror while the infrared source was on the other focal point. The amplitudes were adjusted with an attenuator in front of the sample cell. The chopping frequency was 40 Hz. The second setup was made using an electrically modulated blackbody radiator. Two sources were set just in front of the sample and reference cells. The hot area in the source was approximately 1 mm in diameter. The input voltage was square wave modulated at 15 Hz, giving a modulation of more than 60 % to the optical output. The photoacoustic cell response at 15 Hz was close to the value at 40 Hz. The third setup included a CO_2-laser, chopper and a beamsplitter. The optical power was set to 168 mW using a polarizer and the laser transition was set to 10P(14) at 10.532 μm.

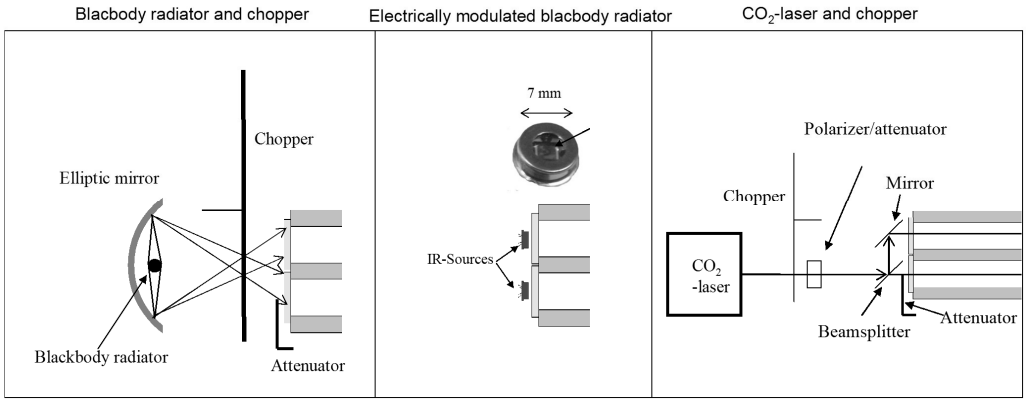

Figure 14. Experimental setups with three different infrared sources.

Ethylene was used as a demonstration gas. The photoacoustic cell was filled with 10 % ethylene in nitrogen, when blackbody sources were used, and a lower 1 % mixture with the laser source due to the signal crossing the upper dynamical limit of the laser interferometer. The ethylene concentration in the sample cell varied from 100 ppm to 1000 ppm. The measured difference signal with the large blackbody source was roughly 40 times higher, and with the CO_2-laser 3300 times higher, than with the electrically modulated blackbody source (Fig. 15). The signal-to-noise ratio with the three setups (1.3 s measurement time) resulted in the corresponding detection limits of 0.92 ppm (Blackbody – chopper), 33 ppm (Blackbody - electric), and 0.010 ppm (CO_2-laser). The experiments are described in Paper [III] and an additional discussion on the comparison of infrared sources is presented in Paper [IV].

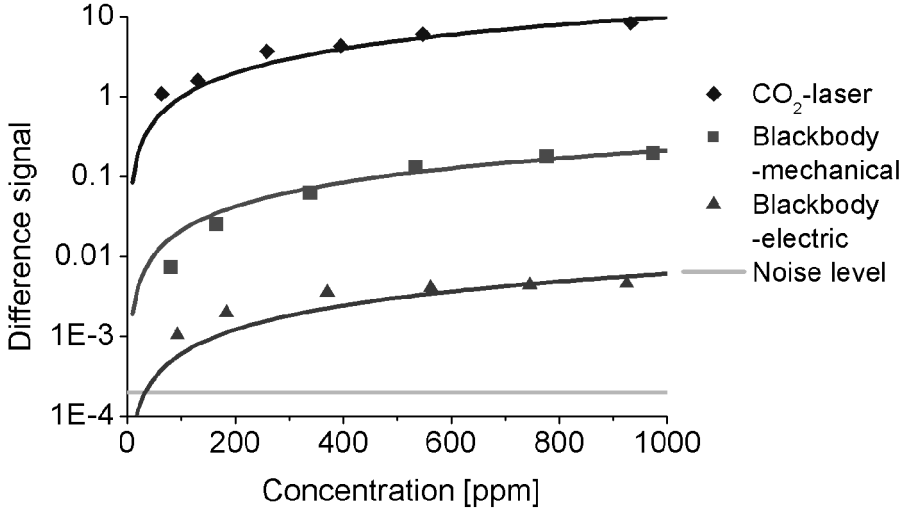

Figure 15. Measured difference signals with the three infrared sources and fitted linear curves

3.3. FTIR setup

FTIR spectroscopy [70] is a suitable technique for when several components have to be analyzed simultaneously and their cross correlation is high. Even if concentrations of different components vary considerably, these components can be separated well. There are certain benefits in photoacoustic FTIR spectroscopy (FTIR PAS) compared to conventional transmission based FTIR spectroscopy. Still very few studies concerning gas-phase photoacoustic FTIR spectroscopy can be found in the literature [71]-[74], since the sensitivity of condenser microphones has been insufficient. Most of the benefits relate to the property of photoacoustics that the absorption is measured directly. If the absorbance is well below 1, the height of spectral line is directly proportional to the concentration Eq. (25). This results in the following features which differ from those obtained during transmission measurements: the signal-to-noise ratio is always higher with increasing absorption, the spectrum is much more immune to baseline distortions, spectra can be scaled and subtracted more easily, the calculation of absorbance spectrum is not necessarily required, and the response is high also with relatively short absorption path lengths. Other advantages of photoacoustics are the small sample volume and constant response to all wavelengths. In Fig. 16 the comparison of the spectrum calculation between conventional transmission FTIR and photoacoustic FTIR

are demonstrated with real measured spectra that contain 100 ppm of CH_4, water and carbon dioxide.

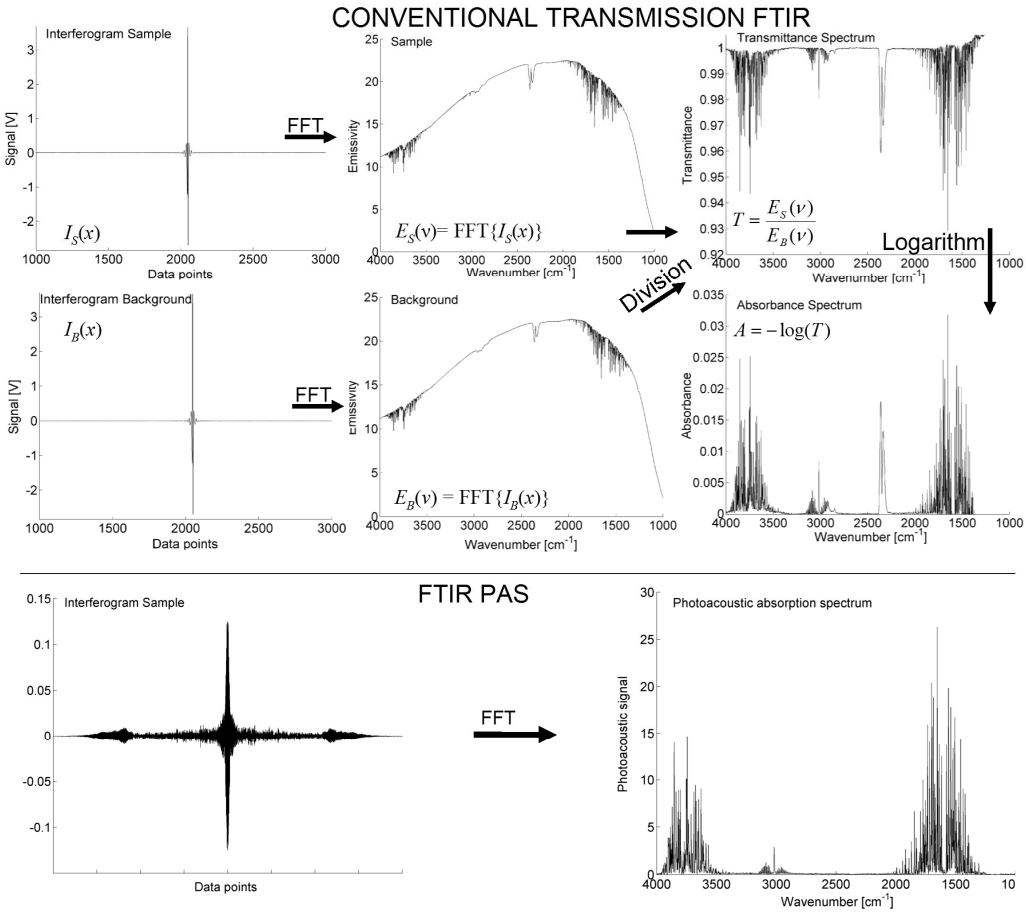

Figure 16. Comparison of the absorption spectrum calculation in conventional transmission and photoacoustic FTIR spectroscopy. Both samples contain 100 ppm of methane.

3.3.1. Formation of the photoacoustic FTIR spectrum

A typical setup of the photoacoustic FTIR spectroscopy for gas-phase samples contains a photoacoustic cell and FTIR interferometer whose output is a collimated beam, which is focused to the photoacoustic cell using an off-axis parabolic mirror (Fig. 17). An interferogram is recorded with the optical cantilever microphone and transformed into a spectrum.

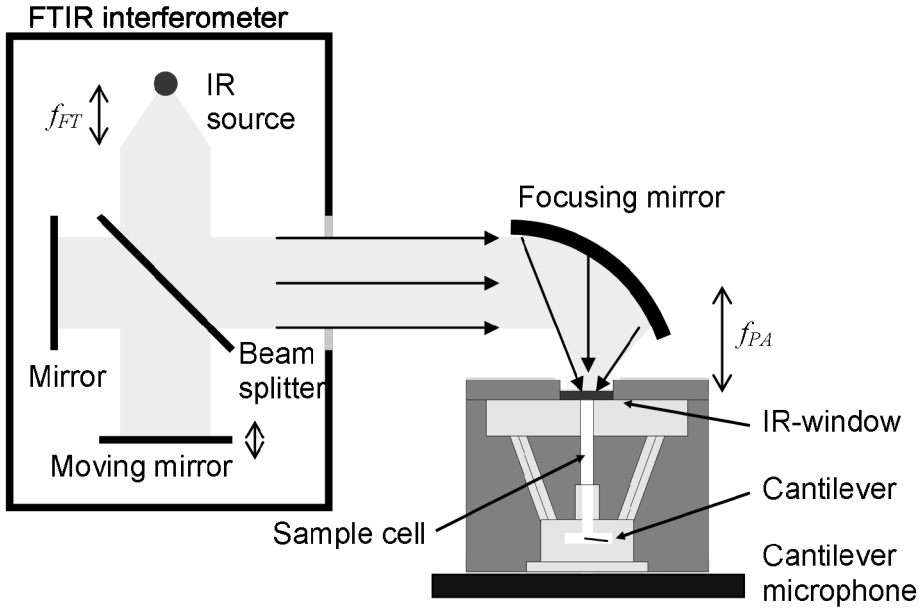

Figure 17. Typical gas-phase FTIR PAS setup with a cantilever microphone.

The photoacoustic infrared spectrum of the multicomponent sample can be written as

$$S_{FTIR}(\nu) = C(\omega)\left[1-\exp\left(-\sum_i E_{A,i}(\nu)p_i l\right)\right]P_0(\nu)T_{BS}(\nu)T_w(\nu)\,, \tag{43}$$

where $P_0(\nu)$ is the power density of the infrared source, p_i is the partial pressure of the component i, $T_{BS}(\nu)$ is the throughput of the interferometer beamsplitter, and $T_w(\nu)$ is the photoacoustic cell window transmittance. The modulation of the infrared radiation intensity is created by moving one of the interferometer mirrors with constant velocity c_{mirror}. The wavenumber is directly proportional to the angular velocity $\omega = 2\pi f$:

$$\nu = \frac{\omega}{c_{mirror}} = \frac{f}{\lambda_{laser} f_{laser}} = \nu_{laser}\frac{f}{f_{laser}}\,. \tag{44}$$

Usually the mirror speed is given as a laser frequency f_{laser}, which corresponds to the modulation frequency of the interferometer using a laser whose wavelength is λ_{laser} and wavenumber ν_{laser}. An example of the wavenumber band variation as a function of wavelength is given in Fig. 18.

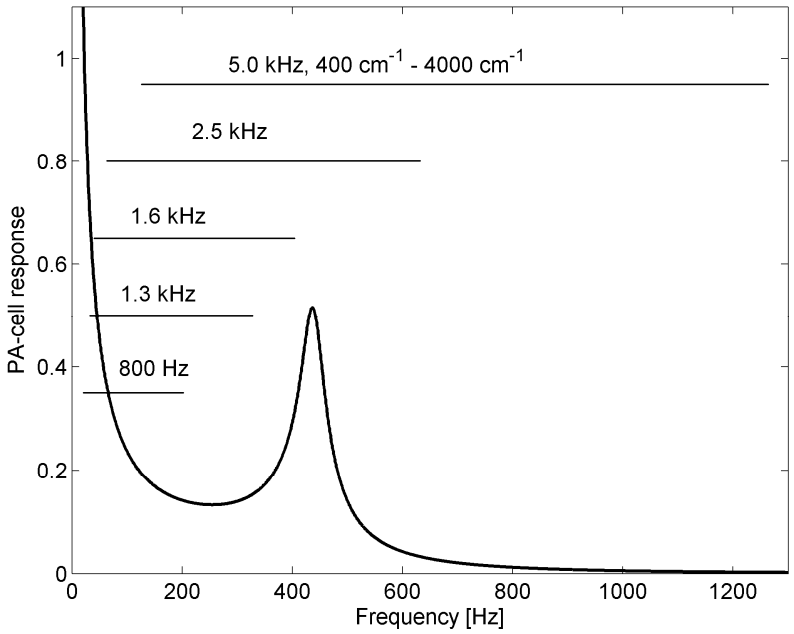

Figure 18. Spectral band of 400 cm^{-1} – 4000 cm^{-1} with different HeNe-laser frequencies and a photoacoustic cell response.

The absorption spectrum $E_A(\nu)$ is a convolution of the interferometer instrument function $W_A(\nu)$ and pressure (or Doppler) broadened absorption spectrum $E(\nu)$

$$E_A(\nu) = W_A(\nu) * E(\nu)\,. \tag{45}$$

When aperture broadening due to the finite infrared source and truncating of the signal are taken into account, the instrument function has the form [75]

$$W_A(\nu) = \Pi_\Omega(\nu) * \delta\left(\nu \mp \frac{\nu_0\Omega}{4\pi}\right) * 2L_{FT}\,\mathrm{sinc}\left(2\pi\nu L_{FT}\right), \tag{46}$$

where $\Pi_\Omega(\nu)$ is a boxcar function whose width is $\delta_\Omega = \nu_0\Omega/2\pi$ and height is $2\pi/\nu_0$, ν_0 is the line center wave number, Dirac's delta function $\delta(\nu - \nu_0\Omega/4\pi)$ describes the shift of the line, Ω is the solid angle where the infrared source is observed, and L_{FT} is the optical path difference at the truncation point. In the case when the truncation of the signal determines the resolution, an additional apodization function W_A is often used in the convolution in Eq. (45) for selecting the line shape in order to avoid shoulders from the sinc-shaped line.

The radiation power density entering the interferometer is derived from Planck's radiation law as follows

$$P_0(\nu) = \varepsilon_0 \frac{2\pi hc^2}{\nu^4\left[\exp(hc\nu/kT)-1\right]} \cdot \frac{a\Omega_0}{2\pi} \propto a\Omega_0 = \Omega A_B = \frac{aA_B}{f_{FT}^2}, \tag{47}$$

where ε_0 is the source emissivity, h is Planck's constant, c is the speed of light, a is the area of the infrared source, Ω_0 is the solid angle where the radiation is collected by the collimating mirror, A_B is the area of the cross section of the collimated beam, and f_{FT} is the effective focal length of the collimating mirror. From Eqs. (46) and (47) it can be seen that the area of the infrared source affects the spectral resolution and power density. The optimal sampling range should be selected so that the full width at half heights (FWHH) of the line shape functions due to truncation, δ_L, and that due to aperture broadening, δ_Ω, are equal

$$\delta_\Omega = \delta_L \quad \Leftrightarrow \quad \frac{\nu_0\Omega}{2\pi} = \frac{1.21}{2L_{FT}} \quad \Leftrightarrow \quad \frac{\nu_0 a}{f_{FT}^2 2\pi} = \frac{1.21}{2L_{FT}}. \tag{48}$$

Since it is possible to choose the diameter d of the photoacoustic cell relatively freely, the signal amplitude can be enhanced remarkably by using a low resolution and a large infrared source and aperture. The diameter should be selected according to the equation

$$d = \sqrt{\frac{4a}{\pi}} \frac{f_{PA}}{f_{FT}}, \tag{49}$$

where f_{PA} is the effective focal length of the focusing mirror (Fig. 17). The photoacoustic methane spectrum with 8 cm^{-1} resolution and components $C(\omega)$, $P_0(\nu)$, $T_{BS}(\nu)$, and $T_w(\nu)$ from Eq. (43) with the mirror speed of 0.08 cm/s are shown in Fig. 19. If step-scan interferometry [76] is used, the spectral response changes so that the cell constant is equal on every wavelength. It gives some enhancement to the signal, because a much lower modulation frequency than for continuous scanning can be selected, thereby giving a higher response.

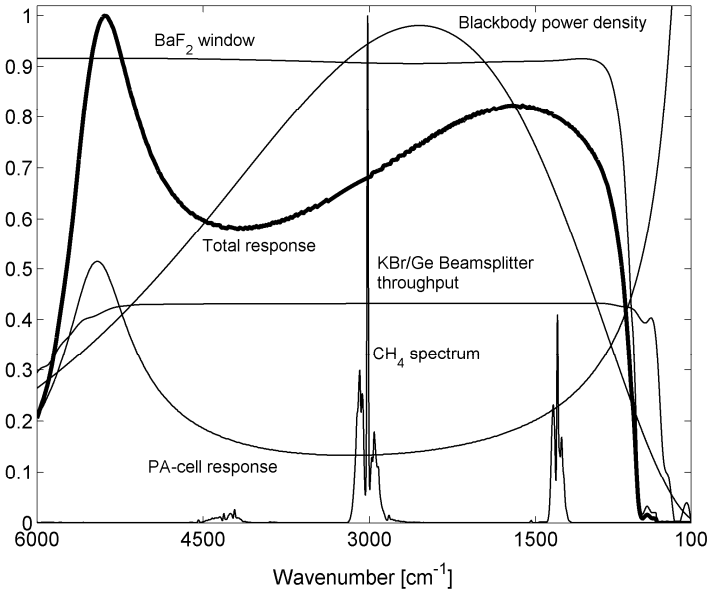

Figure 19. Simulated photoacoustic methane spectrum, at 8 cm^{-1} resolution, and system response.

3.3.2 Spectral errors in gas-phase photoacoustic FTIR spectroscopy

There are several mechanisms that create errors in gas-phase FTIR spectra such as line shape distortions, spectral background distortions, the nonlinearity of Beer's law due to finite resolution, and the signal-to-noise ratio. The errors due to the interferometer are similar for photoacoustics and the conventional transmission method. Since photoacoustics is a direct absorption method, there are some discrepancies in the behavior of some errors. In this chapter the most relevant differences are discussed and some practical examples from simulations are given.

Spectral background distortions in conventional FTIR are caused by the need for the measurement of the background spectrum and another sample spectrum, which are measured separately. If too long a time has elapsed since the background measurement, the blackbody temperature (linear error) or optical alignment (nonlinear error) may have changed, for example, due to the thermal instability of the interferometer, causing baseline errors in the absorbance spectrum. In quantitative analysis these errors have to be compensated [77]. When direct absorption measurement of photoacoustics is used, these instabilities do not cause baseline error, but they distort the total

response of the cell (Fig. 19). This means that the relative height of the absorption lines at different wavenumbers is altered. The effect of the error is small, because it is not amplified by dividing the two spectra. Instead of the instabilities the baseline in photoacoustics is generated by the background signal due to the cell walls and windows. This signal is relatively low and it stays constant in time, so it can be easily measured and subtracted from the sample spectrum.

The nonlinearity of Beer's law means that at high absorbances due to the finite resolution the height of the absorbance spectrum is no longer linearly proportional to the concentration, in other words a higher concentration spectrum cannot be created from lower concentration spectrum by multiplication. Nonlinearity can be determined as [78]

$$\text{nonlinearity} = \frac{\text{CLS result}}{b}, \tag{50}$$

where the term, CLS result, is the coefficient given by the classical least squares fit and b is the ratio between the concentrations of the library spectrum and fitted spectrum. In Fig. 20, the nonlinearity of the water spectrum at a 2 cm^{-1} and 64 cm^{-1} resolution with a 20 cm absorption path length, and the residuals after the subtraction of the fitted library spectrum from the 20000 ppm spectrum, are simulated. The library spectrum is determined using a 100 ppm water concentration. Neither the calculation of absorption, nor a change in the resolution has much of an affect on the nonlinearity of the water spectrum with a 20 cm absorption path length. The effect of nonlinearity is the same in photoacoustics as conventionally, but a shorter absorption path increases the linear range.

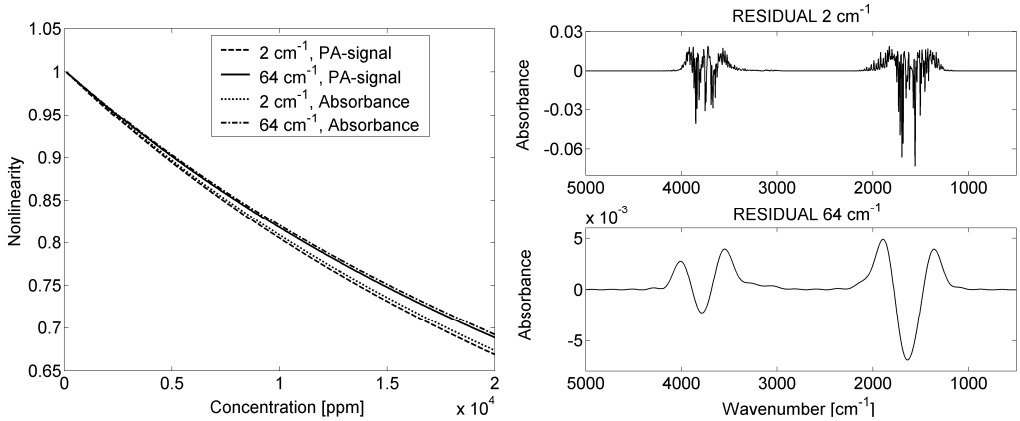

Figure 20. On the left, a simulated nonlinearity of the water spectrum at 2 cm^{-1} and 64 cm^{-1} resolutions and a 20 cm path length due to Beer's law in the

spectrum directly from the photoacoustic signal and calculated absorbance spectrum (10-based logarithm). On the right, there are simulated residuals after the subtraction of the fitted library spectrum from the spectrum of 20000 ppm of water.

In photoacoustic FTIR spectroscopy, the absorbance spectrum $A(\nu)$ (*e*-based) can be calculated from the equation

$$A(\nu) = -\ln\left(1 - \frac{S(\nu)}{g \cdot S_0(\nu)}\right), \tag{51}$$

where S is the sample spectrum and S_0 is the reference spectrum. The reference spectrum has to be measured e.g. by using a solid-phase carbon black sample in the absence of "black gas", and a constant g is used for adjusting the signal level to correspond to that of an ideal gas-phase black absorber. The parameter g can be determined from Eq. (51), if $A(\nu)$ is modeled for a certain concentration and $S(\nu)$ is measured with the same concentration. If the parameter cannot be determined precisely enough, it is better not to calculate the absorbance spectrum, but to use directly the measured spectrum in the quantitative analysis. In the example in Fig. 21, the absorbance is calculated perfectly, when parameter g is correct. When the determined parameter differs from the correct value of g by 10 %, the calculated absorbance spectrum gives more erroneous results than an uncorrected spectrum for concentrations under 3300 ppm. The calculation of the absorbance spectrum of methane is demonstrated in Paper [V].

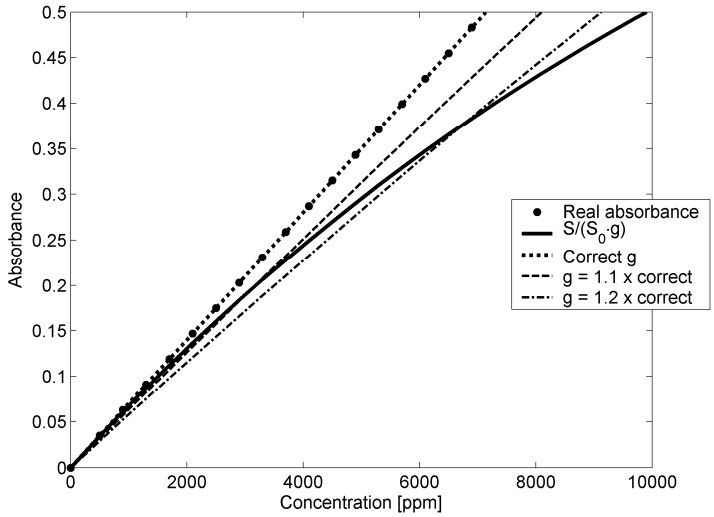

Figure 21. Comparison of absorbances (*e*-based logarithm) calculated using different values of *g*.

The signal-to-noise ratio in photoacoustic FTIR is linearly proportional to the absorption line height, if absorbance is approximated as $A(\nu) \approx S(\nu)/(gS_0(\nu))$. At high absorbances the approximation is no longer valid and a logarithmic correction has to be used, Eq. (51). In this case, the signal-to-noise ratio decrease at line positions is identical for conventional transmission FTIR and photoacoustic FTIR spectroscopy, except that in photoacoustics the absorption path length is always relatively short. The signal-to-noise ratio obtained with a photoacoustic cell of length 7 mm corresponded to that from a 67 mm long transmission cell with a DTGS detector in the study presented in Paper [V]. A shorter absorption path length affects the signal-to-noise ratio at the peak position, as shown in Fig. 22. In the case when the most interesting absorption lines are under strong interfering lines, this effect becomes important. This problem is acknowledged in quantitative analyses of multicomponent gas samples [79].

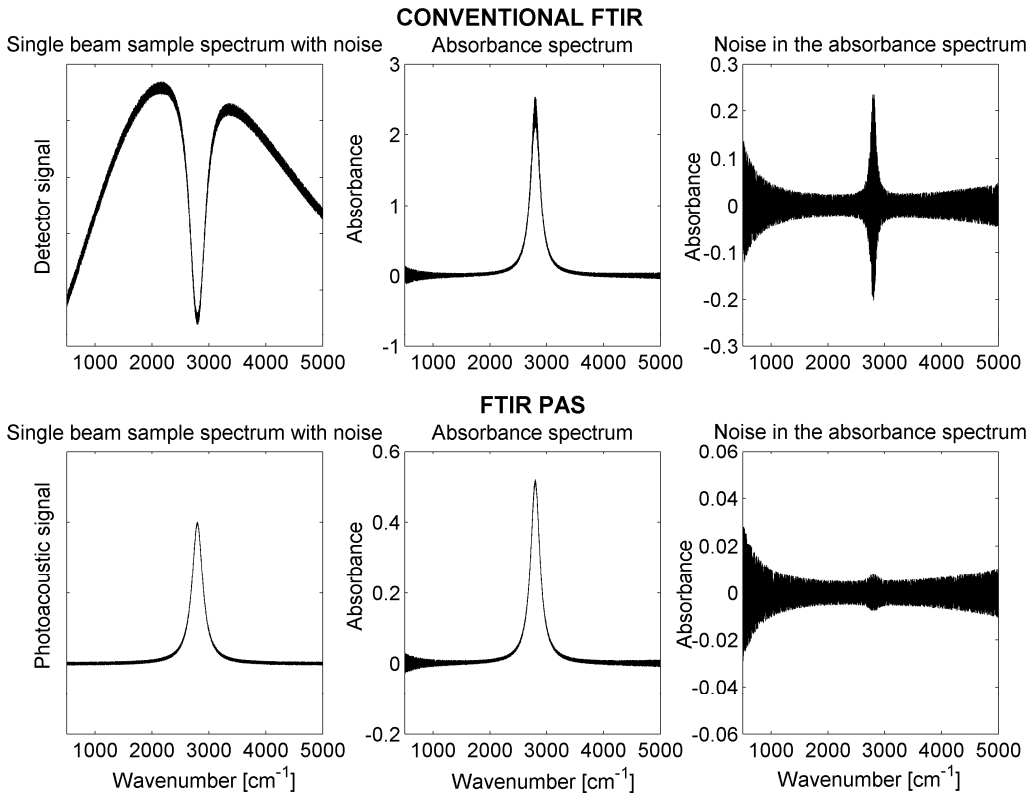

Figure 22. Noise increase at the peak position of the absorbance spectrum (*e*-based) in conventional transmission FTIR and photoacoustic FTIR spectroscopy.

3.3.3. Selectivity and multicomponent measurements

Selectivity in photoacoustic FTIR spectroscopy is obtained by creating a spectral library of the possible components in the sample gas and solving the concentrations using the classical least squares fit (CLS) [80]. Another widely used fitting algorithm, partial least squares regression (PLS), is discussed in [79][81][82]. As an example of the selectivity with simple hydrocarbons in a multicomponent sample, a measured spectrum and fitted library spectra are presented in Fig. 23. It is clear that the different components can be separated from the spectrum with a high degree of accuracy.

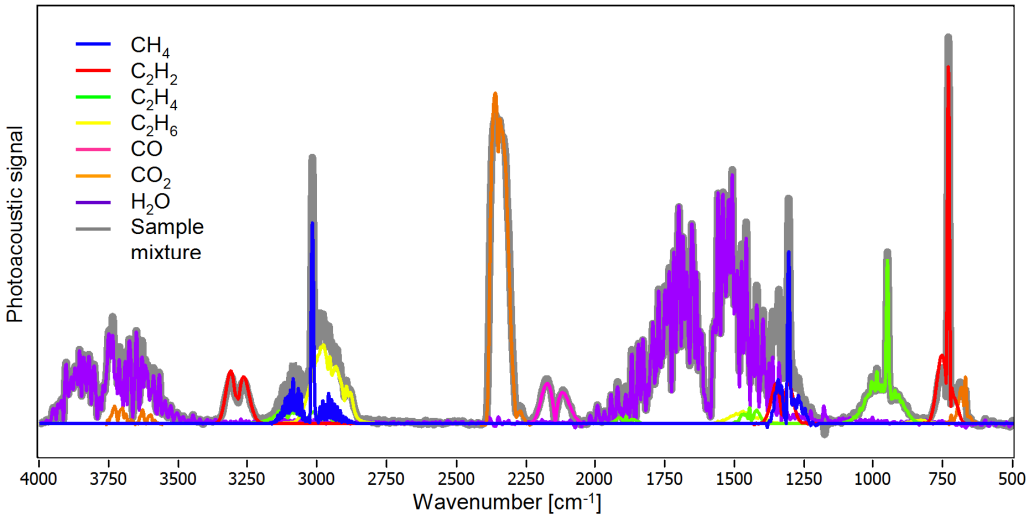

Figure 23. Measured photoacoustic spectrum of multicomponent sample (grey line) and fitted library spectra (colored lines). Concentrations of hydrocarbons and carbon monoxide are between 200 ppm and 400 ppm, water vapor concentration is approximately 6000 ppm and carbon dioxide concentration 1500 ppm.

When detection limits are calculated from the multicomponent sample (Fig. 23), they are around 1 ppm when averaged over 100 scans, depending on the system. The detection limits were calculated as an uncertainty in the result from CLS. The uncertainty was determined as twice an rms-value of the residual weighted by the library spectrum. The detection limits are shown in Table II and relevant system parameters in Table III. The measurements in Fig. 23 are made with System 1 and measurements in Fig. 25 with System 2.

Table II. Measured detection limits of a multicomponent sample with two different FTIR PAS systems. The values in parentheses are not measured, but evaluated according to measured values.

	Detection limit [ppm]	
Gas	System 1	System 2
CH_4	1.2	0.3
C_2H_2	0.6	(0.15)
C_2H_4	1.2	(0.3)
C_2H_6	0.6	(0.15)
CO_2	4	0.5
CO	0.8	(0.2)
H_2O	10	1

Table III. Relevant system parameters in the detection limit measurement.

System parameter	System 1	System 2
FTIR interferometer	Interspectrum 401-X	Bruker IR-Cube Matrix MF
Source diameter [mm]	6	4
HeNe laser freq. [kHz]	2.5	1.6
Beam diameter [mm]	38	25
Spot diameter on focus [mm]	2.9	4.4
resolution [cm^{-1}]	8	4
$a\Omega_0$ [mm^2]	5.1	1.3
Number of scans	100	100
Cell diameter [mm]	3	4.5
Cell length [mm]	20	100
Cell pressure [mbar]	1000	480
Cantilever length [mm]	4	6
Cantilever width [mm]	1.5	1.5
Cantilever thickness [mm]	10	10
Cantilever frame gap [µm]	3	3

Also components that are fully overlapping with other spectra can be distinguished. For example the nitric oxide spectrum can be easily separated from the water spectrum (Fig. 24). Another example is presented in Fig. 25 where a spectrum of the sample that contains 1200 ppm of water and 100 ppm of methane is shown before and after water subtraction. The water library

spectrum was made with 700 ppm of water leaving a residual after subtraction at the level equal to noise averaged over 100 scans. A negative residual in the left-hand-side spectrum of Fig. 25 is due to the carbon dioxide spectrum included in the library. The components in the sample mixture should be known so that only the required spectra in the library are used with CLS – no more, no less.

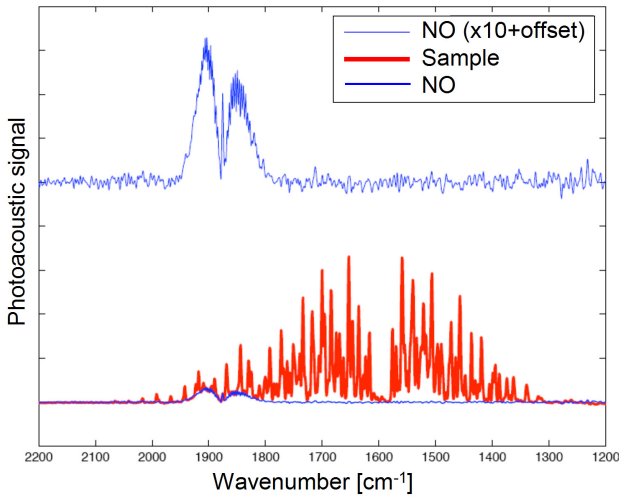

Figure 24. Measured photoacoustic spectrum of 90 ppm of nitric oxide (NO) and water mixture and pure NO spectrum after water subtraction.

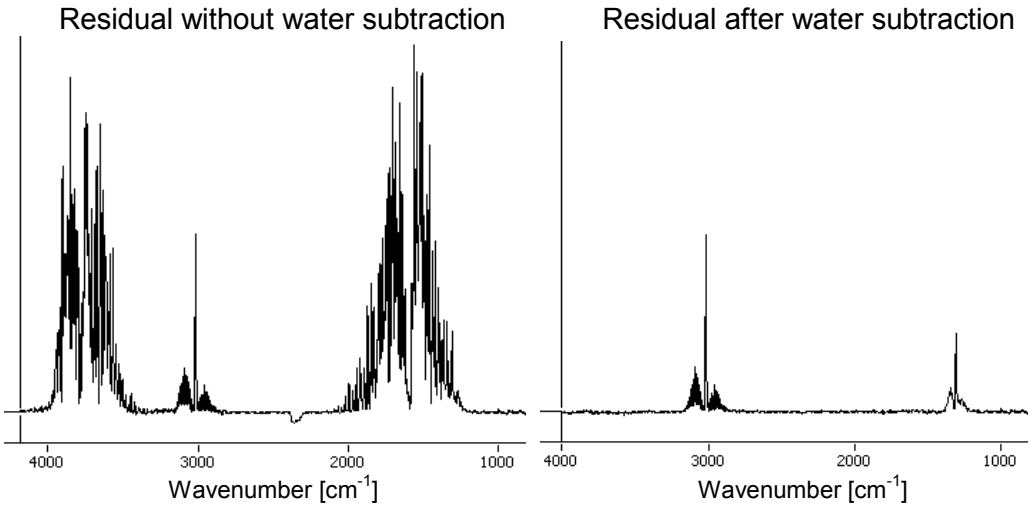

Figure 25. Residuals of mixture containing 100 ppm of methane and 1200 ppm of water, when only carbon dioxide is in the library and after water is added to the library.

3.3.4. Optimization of the FTIR system parameters

Optimization of the system should follow the pattern: maximize the optical power, and design the cell and cantilever dimensions according to the FTIR interferometer and the application. First, the value $a\Omega_0$ of the FTIR interferometer can be optimized according to the desired resolution of the application. Often a low resolution is suitable for quantitative measurements [83]. The lower the resolution, the larger the infrared source can be (Eq. 48). The optical power entering the photoacoustic cell increases linearly, when the resolution is decreased and source area increased. The focal length of the focusing mirror is chosen by keeping in mind the magnification of the infrared source image, spot size on the photoacoustic cell window, and angular distribution where the radiation is entering in the photoacoustic cell.

The cell diameter is selected to be equal to the spot size. The signal-to-noise ratio decreases roughly linearly with the cell diameter, when the cell diameter is increased over the spot size, and respectively decreases roughly in proportion to the second power, when it is decreased below spot size. Next the cell length is selected. The signal-to-noise ratio has a maximum value with one cell length for each set of dimensions of the cantilever in different pressures. The nonlinearity of the spectrum and finite reflectance of the cell walls limits the possible cell length.

Cantilever dimensions are basically limited by manufacturing. The cantilever should be as long as possible and as thin as possible. The ratio of these two dimensions has a great effect on optimization, since the cantilever string constant is proportional in the third power to the ratio. However, it is limited to 500 by manufacturing in order to prevent the cantilever from bending too much. The optimal cantilever width depends on the other cantilever dimensions and cell volume, so that the minimum width allows the laser beam to be easily adjusted to the cantilever end without touching the frame gap. The frame gap should simply be as small as possible. By using different cantilever dimensions the resonance frequency can be set. This frequency is, in some cases, determined by the wavelength range and mirror velocity to be used. In Fig. 26 the signal-to-noise ratio is simulated for the photoacoustic cells described in Table III. The Brownian noise is assumed to be dominating and also low constant level electronic noise is assumed. The drop of the signal-to-noise ratio after the resonance frequency and the ability to select possible measurement ranges are well demonstrated.

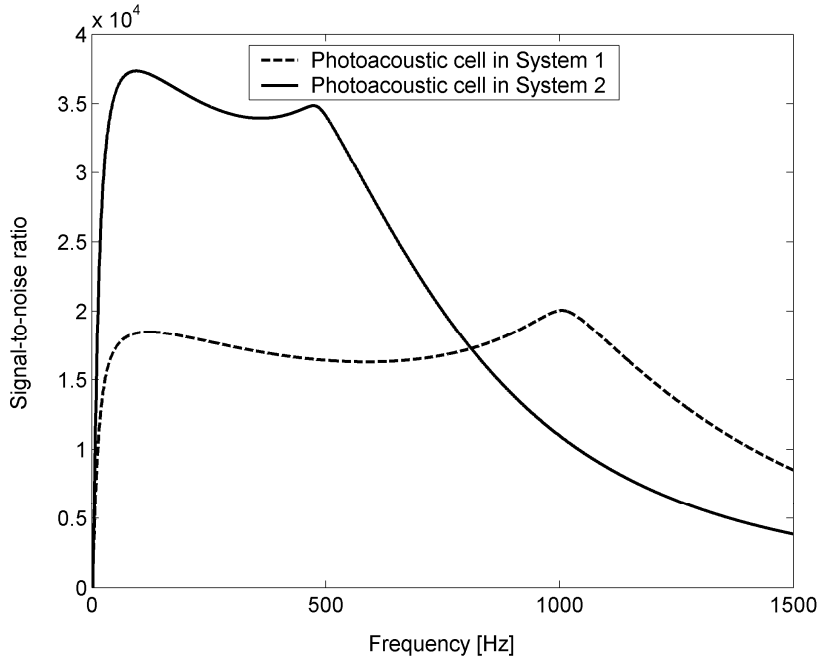

Figure 26. Simulated signal-to-noise ratio as a function of modulation frequency of the two photoacoustic cells described in Table III.

Chapter 4

Photoacoustic FTIR spectroscopy of solid- and liquid-phase samples

4.1. Signal generation in solid- and liquid-phase samples

The principle of signal generation is similar for solid- and liquid-phase samples. Periodic heating in the sample is generated by the absorption of the infrared radiation. The periodic heat flow to the gas from the sample surface generates expansion and contraction in a thin layer of gas close to the surface. This mechanism is thermal coupling [28]. Periodic heating of the sample causes also pressure variations to propagate all directions, and a superposition of these acoustic waves at the sample surface generates a surface motion that is coupled to the surrounding gas. This mechanism is called acoustic coupling [29]. The signal detected in the gas by the cantilever is a combination of these two mechanisms. This combination is called a composite piston [29]. In a typical solid-phase photoacoustic experiment, thermal coupling is dominant and acoustic coupling can be neglected. Acoustic coupling can be the dominating mechanism for some liquids. The complex pressure signal amplitude for thermally thick samples according to composit piston model [29] is given as

$$p(\omega) = -\frac{j}{\omega}\frac{\gamma p_0}{l_g}\frac{I_0(\nu)}{2\rho_s C_{ps}}\left(\frac{\alpha(\nu)}{\sigma_g T_0 (g+1)(r+1)} + \beta_T\left[1-\exp(-\alpha(\nu)l_s)\right]\right), \quad (52)$$

where j is an imaginary unit describing the phase of the signal, ω is the angular frequency of the modulation, l_g and γ are the thickness and ratio of specific heat capacities of the gas, p_0 and T_0 are the gas pressure and temperature, I_0 is the incident radiation intensity at wavenumber ν, ρ_s and C_{ps} are the density and

heat capacity of the sample, α is the absorption coefficient of the sample, l_s is the thickness of the sample, β_T is the (volume) coefficient for thermal expansion, $g = (K_g\sigma_g)/(K_s\sigma_s)$, $\sigma_g = (j\omega/D_g)^{1/2}$, $\sigma_s = (j\omega/D_s)^{1/2}$, $r = \alpha/\sigma_s$, D_g and D_s are the thermal diffusivities of the gas and sample, and K_g and K_s are the thermal conductivities of the gas and sample. The first term in parentheses in Eq. (52) describes thermal coupling and the second term acoustic coupling. When an absolute value of the pressure signal amplitude and the force affecting the cantilever, Eq. (10), are calculated and the force is substituted into Eq. (6), the signal amplitude response in a solid-phase photoacoustic system with a cantilever microphone can be given as

$$A(\omega) = \frac{A_C \gamma p_0}{\omega V} \frac{P_0(\nu)}{2\rho_s C_{ps}} \left(\frac{\alpha(\nu)}{\sigma_g T_0 (g+1)\sqrt{r^2+1}} + \beta_T \left[1 - \exp(-\alpha(\nu) l_s)\right] \right) \times \frac{1}{m\sqrt{(\omega_0^2 - \omega^2)^2 + (\omega D/m)^2}} \frac{\omega\tau_{23}}{\sqrt{1+(\omega\tau_{23})^2}}. \quad (53)$$

The leak through the cantilever is still modeled using a highpass filter, but the heating of the sample and molecular relaxation times are included in the composit piston model that describes them only with a simple 1/ω-dependence. Optically opaque and thermally thick samples that have a large surface area give high signals. Helium is ideal for the gas medium, since it has a high thermal diffusivity.

The signal detected by the cantilever is produced above a certain depth from the sample surface. Either optical or thermal decay length limits the sampling depth (Fig. 27). If the sample is optically opaque, roughly 63 % (1-1/*e*) of the signal is generated before the depth $l = 1/\alpha$ from the surface, where α is the absorption coefficient of the sample. Respectively, if the sample is thermally thick, 63 % of the signal is generated before the depth limited by the thermal diffusion length

$$\mu = \sqrt{\frac{2K}{\omega\rho c_p}}, \quad (54)$$

where K is the thermal conductivity, ρ is the density and c_p is the specific heat capacity of the sample, and ω is the angular frequency of the intensity modulation. The temperature difference of the gas layer on the surface is the combination of these two decays and can be described as [19]

$$\Delta T_{gas} = I_0(1-R)(1-R_T)\alpha \exp\left(-\alpha l + \frac{l}{\mu}\right)\mathrm{d}l\,, \tag{55}$$

where I_0 is the intensity of the incident infrared radiation, R is the reflectance of the radiation from the sample surface, R_T is the reflectance of the thermal wave from the sample surface, and l is the depth from the sample surface. This means that the sampling depth ($\mu << 1/\alpha$) can be varied by changing the FTIR interferometer mirror velocity and modulation frequency. Another way to look at this is that optical saturation can be avoided by using high modulation frequencies and short sampling depth. The phase lag due to the finite propagation time might decrease the signal level and it is the third thing that limits the sampling depth. The maximum depth on the length scale is $2\pi\mu$, which corresponds to the phase lag of 360 degrees [17].

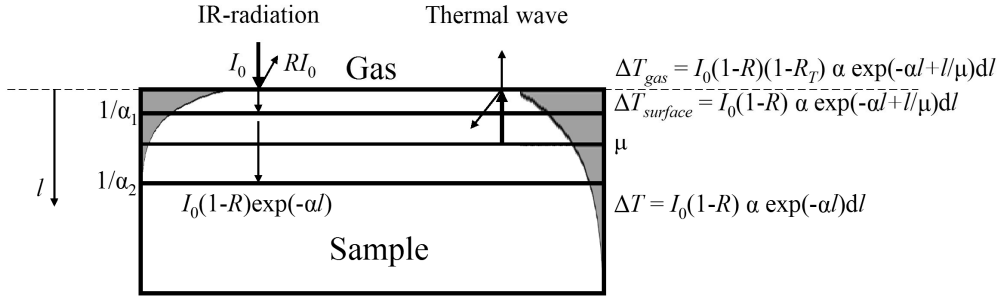

Figure 27. Schematic drawing of the optical and thermal decay length influence on the sampling depth. The sampling depth is limited by the thermal diffusion length, if it is higher than absorption depth $\mu << 1/\alpha_2$, and by the absorption depth in the case when $1/\alpha_1 << \mu$.

The effects of the interferometer and windows wavelength response and photoacoustic cell frequency response on the spectrum (Fig. 19) can be compensated by the normalization of the signal. For normalization, a reference spectrum must be measured using a constant absorbent such as a carbon black coated film. With samples that have low absorption coefficients the normalization is performed simply by dividing the sample single beam spectrum by the reference spectrum. Linearization corrects also the saturation effect and line shape of the spectra with high and low absorption coefficients. For linearization, either Eq. (51) can be used or we can employ the following formula [84][85]

$$S_L = \frac{S_R^2 + S_I^2}{\sqrt{2}(S_I R_R - S_R R_I)}, \tag{56}$$

where S_L is the linearized spectrum, S_R and S_I are the real and imaginary components of the sample spectrum and R_R and R_I are the real and imaginary components of the reference spectrum. If Eq. (56) is used, shifting of the interferograms might be required in order to have equal centerburst retardations [17]. Linearization might be important with quantitative analyses or spectral library searches from general libraries. For example, transmission spectra libraries can be used for identifying photoacoustic spectra [19].

4.2. Photoacoustic cell design

In order to optimize the signal-to-noise ratio, the photoacoustic cell must be designed so as to minimize the cell volume. The cantilever dimensions have to be selected according to this volume. Again the ratio of the cantilever length and thickness confines the signal. In Fig. 28 the signal response with four different combinations of the cell and cantilever dimensions is simulated using Eq. (53). When the volume of the cell is already very small (line1), an additional decrease does not enhance the signal anymore (line 3), because the gas string is dominating the string constant. On the contrary the scaling of the cantilever dimensions down enhances the signal (line 4) and in this case also the decrease of the volume of the cell increases the response (line 2).

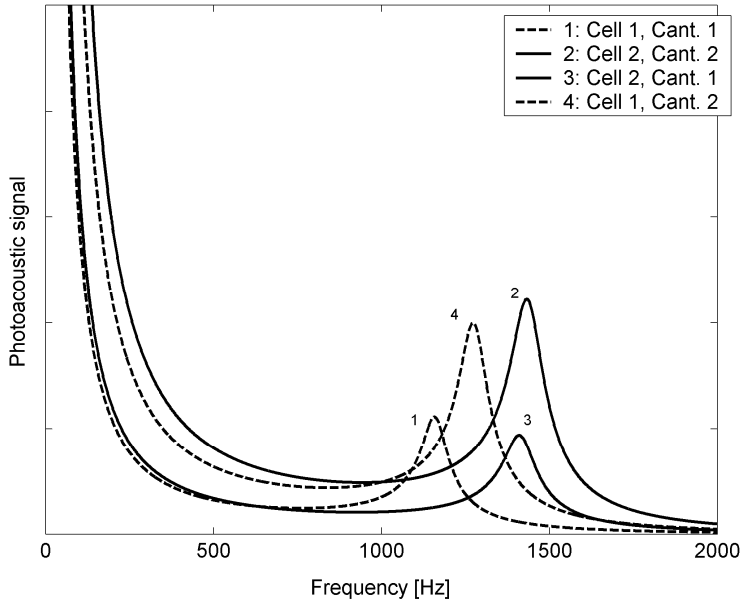

Figure 28. Simulated signal frequency response of the photoacoustic cell with different combinations of two cantilevers and two cell dimensions. The

simulation is made according to Eq. (53) assuming helium atmosphere. Cantilever dimensions were (l_c x w x h, and gap) Cant.1: 4 mm x 1.5 mm x 10 μm, and gap 4 μm, Cant. 2 : 2 mm x 0.8 mm x 4 μm, and gap 1 μm, the volume of the Cell 1 was 0.41 ml and volume of the Cell 2 was 0.25 ml.

A prototype of the photoacoustic cell was made for experimental measurements (Fig. 29). The cell consists of the sample holder, sample cell, cantilever, and balance cell. The samples were set on a small plate at a distance between 1 mm and 2.5 mm from the window. An infrared beam from an FTIR interferometer was focused to the beam guide pipe. The cantilever and sample cell dimensions are the same as for Cant. 1 and Cell 1 in Fig. 28.

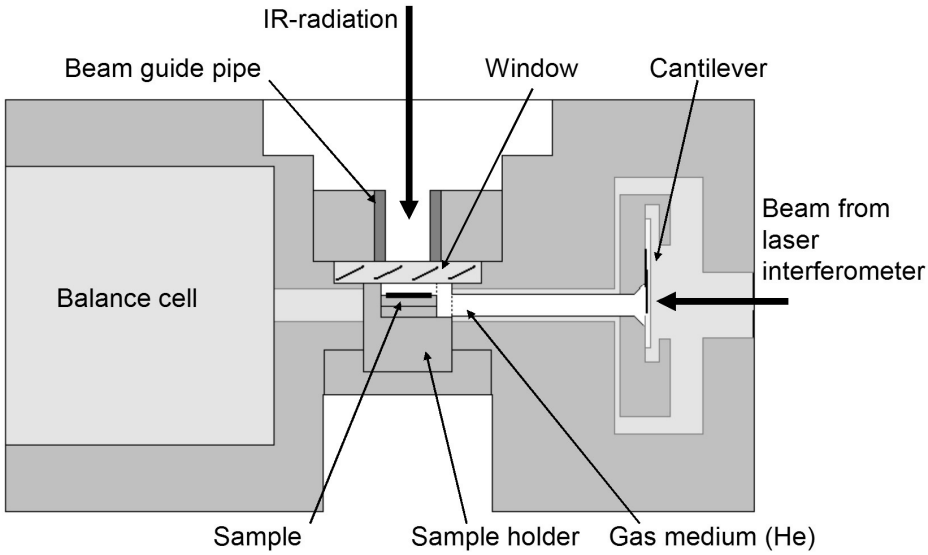

Figure 29. A drawing of the photoacoustic cell made for solid- and liquid-phase samples.

4.3. Photoacoustic cell performance

The measurement of solid- and liquid-phase spectra was demonstrated using the photoacoustic cell (Cantilever PAS) shown in Fig. 29. The cell performance was evaluated by comparing the signal-to-noise ratio of the spectra to that of the reference spectra measured with a commercial photoacoustic detector, MTEC model 300 [86] (Reference PAS). The samples used were a standard carbon black coated film [86], polyethene, and sunflower oil. The FTIR interferometer used in the measurements was the Mattson Galaxy 6020. The interferometer driving parameters are shown in Table IV. The measurements of carbon black, polyethene, and sunflower oil are described also in Paper [V].

Table IV. Measurement parameters.

Parameter	Value
Number of scans	100
Resolution due to drive length [cm^{-1}]	8
Resolution due to source aperture [cm^{-1}]	4 at 3095
Laser frequency [kHz]	1.6
OPD mirror velocity [cm/s]	0.09
Measurement time [s]	168
Pressure in the photoacoustic cell (He) [mbar]	1005

The background single channel spectra measured with the Cantilever PAS, Reference PAS, and DTGS detector of the FTIR interferometer are shown in Fig. 30. The maximum amplitudes of the spectra are scaled to one. With the Cantilever PAS and Reference PAS detectors the background was measured by using standard carbon black coated film. Minor differences in the background spectra are due to the different frequency and wavelength responses of the detectors, and in the low wavenumbers due to the different windows in the detectors.

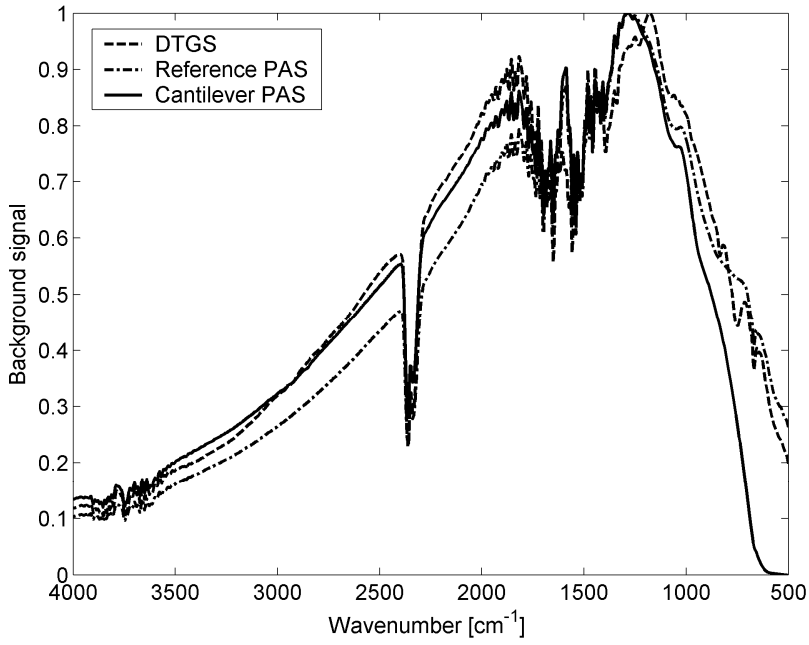

Figure 30. Measured standard carbon black coated film spectra with Cantilever PAS and Reference PAS detectors and single beam background spectrum of DTGS detector.

The signal-to-noise ratio of the background spectra was determined from a 100 % line, which was calculated by normalizing the 10-scans background spectrum with another 10-scans background spectrum. The 100 % lines of the three detectors are shown in Fig. 31. The signal-to-noise ratio was calculated from rms-noise σ at around 2000 cm^{-1} as SNR = 1/2σ. The Cantilever PAS detector gave a 5 times higher signal-to-noise ratio than the Reference PAS detector, but it was 1.3 times lower than for DTGS.

The Cantilever PAS cell could also work as an infrared detector in the same way as Golay-cells [87]. This Cantilever PAS cell is nearly as good a detector as DTGS at mid-IR frequencies, but it works also with shorter and longer wavelengths if the window material is changed. If the cell were to be modified slightly, e.g. as for combination 2 in Fig. 28, it would give a high performance also at mid-IR wavelengths. The modulation frequency is limited due to the photoacoustic cell frequency response, but the response would limit the performance and measurement speed only for short wavelengths. The detector would be especially suited to far-IR wavelengths.

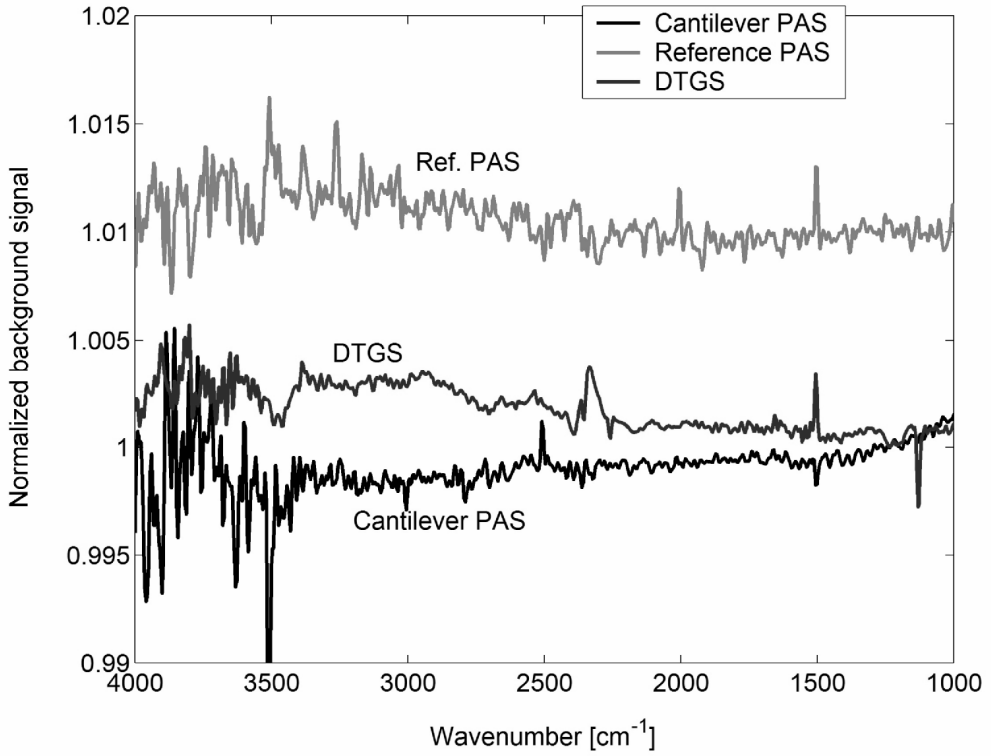

Figure 31. Comparison of 100 % lines with Cantilever PAS, Reference PAS and DTGS detectors.

Polyethene was chosen as a solid-phase sample. In Fig. 32, the measured polyethene spectra with Cantilever PAS and Reference PAS detectors are shown. The signal-to-noise ratio was evaluated from the peak height at 1466 cm^{-1}, and peak-to-peak noise from the range between 2050 cm^{-1} – 2450 cm^{-1}. The signal-to-noise ratio of the Cantilever PAS was 8 times higher than that of the Reference PAS. The normalization of the spectrum was demonstrated by dividing the spectrum measured with the Cantilever PAS by its background spectrum. The polyethene sample also contained a small amount of carbon, which created a broad spectrum under the polyethene lines. In the normalized spectrum it can be seen as an offset level (Fig. 32).

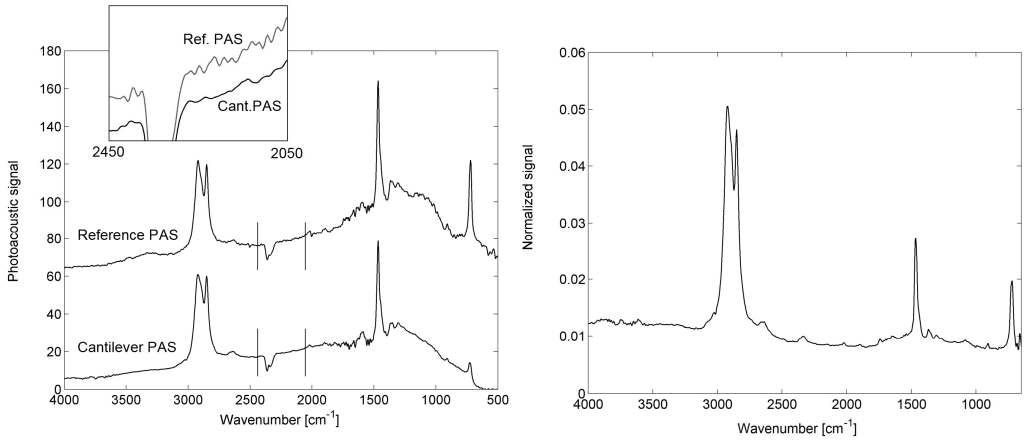

Figure 32. Comparison of polyethene spectra with Cantilever PAS and Reference PAS detectors and normalized polyethene spectrum.

Sunflower oil was taken as a liquid-phase sample. It's spectrum was also measured with both photoacoustic detectors, and the signal-to-noise ratio was evaluated as for polyethene. The peak height was taken at 1746 cm^{-1} and noise evaluated from the band between 1900 cm^{-1} – 2300 cm^{-1}. Cantilever PAS detector had a 10 times higher signal-to-noise ratio than the Reference PAS detector. The measured spectra of sunflower oil are shown in Fig. 33, and the comparison of signal-to-noise ratios of the detectors with carbon black, polyethene, and sunflower oil samples is presented in Table V.

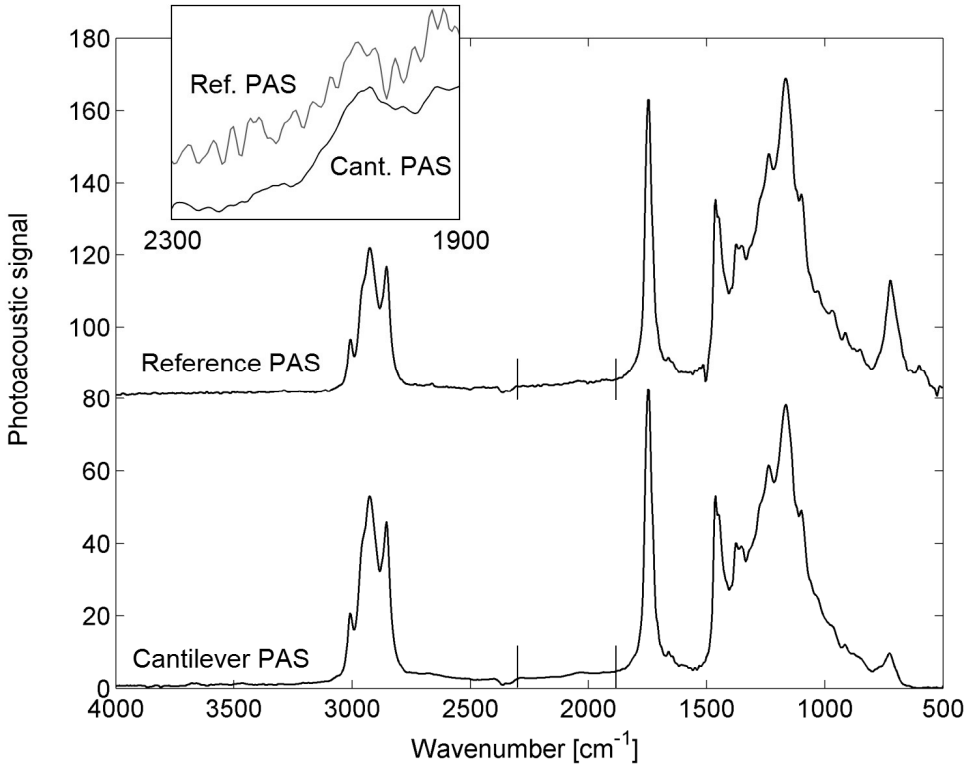

Figure 33. Comparison of sunflower oil spectra with Cantilever PAS and Reference PAS detectors.

Table V. Signal-to-noise ratio comparison of the carbon black, polyethene, and sunflower oil samples with different detectors.

	Signal-to-noise ratio		
Detector	100 % line	Polyethene	Sunflower oil
Cantilever PAS	3480	1060	1550
Reference PAS	679	134	155
DTGS	4683	-	-

Chapter 5

Conclusions

Several prototypes of differential photoacoustic, gas-phase FTIR, and solid-phase FTIR systems were built. Their selectivity and sensitivity were studied and demonstrated by measurements and simulations. The cantilever microphone proved to be suitable for each setup, and will bring advantages compared to existing devices and the use of condenser microphones in many applications. Naturally, the measurement technique should be selected according to the requirements of the application. The cantilever and photoacoustic cell optimization is different in each system.

Three differential photoacoustic system prototypes were built and their sensitivity and selectivity were studied experimentally and theoretically. The differential setup is suitable for online measurements of a single gas component and the measurements can be made from the flowing a sample or even in the open air. The sensitivity is well comparable to that of existing devices; a low ppm range can be achieved with sampling intervals of a few seconds using a blackbody radiator as an infrared source. The selection of the infrared source has a large effect on the sensitivity. The lowest detection limits are achieved, when high power lasers for mid-IR range fundamental vibration lines are used. Selectivity depends strongly on the gas to be measured and other possible components in the sample. For multicomponent samples, a better selectivity is achieved using the FTIR setup.

The gas-phase photoacoustic FTIR setup was studied using four different prototypes, and they were combined with three different kinds of interferometer. The benefits of the photoacoustic FTIR are best exploited, when the interferometer has a slow mirror velocity and a large aperture. These benefits are a high sensitivity from small sample volumes and a short absorption path length, which makes the spectra more linear for higher concentrations and enhances selectivity by allowing, for example, a more accurate water spectrum subtraction. FTIR systems should be used, when many components have to be analyzed simultaneously or when the sample

includes several interfering components. It takes over ten times longer to achieve ppm-level detection limits for a single gas than with the differential system. The measurements cannot be performed during the sample change, but the photoacoustic cell has to be closed while the measurement is on.

The prototype of a detector for solid-phase photoacoustic FTIR spectroscopy was compared to a commercial device. With the cantilever enhanced detector, the signal-to-noise ratios of three samples were 5 – 10 times higher than those obtained with the reference detector, which had a condenser microphone. In terms of the measurement time, this would mean a 25 – 100 times faster measurement in order to achieve the same sensitivity. The sensitivity would still be higher even if air were used as the gas medium instead of helium. Another advantage, compared to existing devices, is the possibility of heating the sensor. This may give new possibilities in research and create new applications.

In the future there will be complete photoacoustic analyzers including several simultaneous infrared sources and miniaturized cells with cantilevers of scaled dimensions. Also new types of laser interferometers to improve the stability of optical microphones, cell heating and optimized FTIR interferometers for photoacoustics will be studied. According to simulations further enhancements in sensitivity can be expected. The use of an optical cantilever microphone has a very promising future in photoacoustic spectroscopy.

Bibliography

[1] C. K. N. Patel, "Laser photoacoustic spectroscopy helps fight terrorism: High sensitivity detection of chemical warfare agent and explosives", *Eur. Phys. J. Special Topics*, **153**, 1, 2008.

[2] Y. Sun and K. Y. Ong, *Detection Technologies for Chemical Warfare Agents and Toxic Vapors,* CRC press, Boca Raton, London, 2005.

[3] W. M. Sigrist, *Air Monitoring by Spectroscopic Techniques*, Chemical Analysis, **127**, Wiley, New York, 1994.

[4] Dwayne E. Heard, *Analytical Techniques for Atmospheric Measurement*, Blackwell Publishing, 2006.

[5] *Measurement of Greenhouse Gases using the Multi-Gas Monitor*, Application note, Innova AirTech Instruments, http://www.innova.dk/uploads/media/Aplic_Greenhouse_Innova.pdf, (available online December 15th, 2008).

[6] M. W. Sigrist, "Trace gas monitoring by laser photoacoustic spectroscopy and related techniques", *Rev. Sci. Instrum.* **74**, 486, 2003.

[7] M. McCurdy, Y. Bakhirkin, G. Wysocki and F. Tittel, "Recent advances of laser spectroscopy based techniques for applications in breath analysis", *Journal of Breath Research* **1**, 014001, 2007.

[8] F. K. Tittel, G. Wysocki, A. Kosterev and Y. Bakhirkin, *Semiconductor Laser Based Trace Gas Sensor Technology: Recent Advances and Applications*, in M. Ebrahim-Zadeh and I. T. Sorokina (Eds.), Mid-Infrared Coherent Sources and Applications, Springer, 467, 2008.

[9] *Direct Industry - Virtual Industrial Exhibition*, http://www.directindustry.com/cat/analysis-and-material-characterisation-test-rigs-I.html., (available online, December 15th, 2008).

[10] A. Rosencwaig, *Photoacoustics and Photoacoustic Spectroscopy*, Wiley, New York, 1980.

[11] F. J. M. Harren, G. Cotti, J. Oomens and S. te Lintel Hekkert, *Photoacoustic Spectroscopy in Trace Gas Monitoring*, in R.A.Meyers (Ed.), Encyclopedia of Analytical Chemistry, Wiley, Chichester, 2203, 2000.

[12] J. Kauppinen, K. Wilcken, I. Kauppinen and V. Koskinen, "High sensitivity in gas analysis with photoacoustic detection", *Microchem. J.* **76**, 151, 2004.

[13] K. Wilcken and J. Kauppinen, "Optimization of a microphone for photoacoustic spectroscopy" *Appl. Spectrosc.* **57**, 1087, 2003.

[14] R. E. Lindley, A. M. Parkes, K. A. Keen, E. D. McNaghten and A. J. Orr-Ewing, "A sensitivity comparison of three photoacoustic cells containing a single microphone, a differential dual microphone or a cantilever pressure sensor", *Appl. Phys. B* **86**, 707, 2007.

[15] T. Kuusela and J. Kauppinen, "Photoacoustic gas analysis using interferometric cantilever microphone", *Appl. Spectrosc. Rev.* **42**, 443, 2007.

[16] V. Koskinen, J. Fonsen, K. Roth and J. Kauppinen, "Progress in cantilever enhanced photoacoustic spectroscopy", *Vibr. Spectrosc.* **48**, 16, 2008.

[17] J. F. McClelland, R. W. Jones and S. J. Bajic, *Photoacoustic Spectroscopy*, in Handbook of Vibrational Spectroscopy, J. M. Chalmers and P. R. Griffiths (Eds.), John Wiley & Sons Ltd., London, vol. 2, 1231, 2002.

[18] K. H. Michaelian, *Photoacoustic Infrared Spectroscopy*, in J. D. Winefordner (Ed.), Chemical Analysis, A Series of Monographs on analytical Chemistry and Its Applications, John Wiley & Sons Inc., Hoboken, NJ, vol. 159, 2003.

[19] J. F. McClelland, R. W. Jones, S. Luo and L. M. Seaverson, *A Practical Guide to FTIR Photoacoustic Spectroscopy*, in P. B. Coleman (Ed.), Practical Sampling Techniques for Infrared Analysis, CRC Press, Boca Raton, FL, 1993.

[20] D. W. Vidrine, "Photoacoustic Fourier-transform infra-red spectroscopy of solid samples", *Appl. Spectrosc.* **34**, 314, 1980.

[21] A. G. Bell, "On the production and reproduction of sound by light", *Am. J. Sci.* **20**, 305, 1880.

[22] A. G. Bell, "Upon the production of sound by radiant energy", *Philos. Mag.* **11**, 510, 1881.

[23] M. L. Viengerov, "Eine Methode der Gasanalyze beruhend auf dem optisch- akustischen Tyndall-. Röntgeneffekt", *Dokl. Akad. Nauk SSSR* **19**, 687, 1938.

[24] K. F. Luft, "Über eine neue Methode der registrierenden Gasanalyse mit Hilfe der Absorption ultraroter Strahlen onhe spektrale Zerlegung", *Z. Tech. Phys.* **24**, 97, 1943.

[25] E. L. Kerr and J. G. Atwood, "The laser illuminated absorptivity spectrophone: a method for measurement of weak absorptivity in gases at laser wavelengths", *Appl. Opt.* **7**, 915, 1968.

[26] L. B. Kreuzer, "Ultralow gas concentration infrared absorption spectroscopy", *J. Appl. Phys.* **42**, 2934, 1971.

[27] J. G. Parker, "Optical absorption in glass: Investigation using an acoustic technique", *Appl. Opt.* **12**, 2974, 1973.

[28] A. Rosencwaig and A. Gersho, "Theory of the photoacoustic effect with solids", *J. Appl. Phys.* **47**, 64, 1975.

[29] F. A. McDonald and G. C. Wetsel, "Generalized theory of the photoacoustic effect", *J. Appl. Phys.* **49**, 2313, 1978.

[30] A. Kosterev, G. Wysocki, Y. Bakhirkin, S. So, R. Lewicki, F. Tittel and R. F. Curl, "Application of quantum cascade lasers to trace gas analysis", *Appl. Phys. B* **90**, 165, 2008.

[31] V. A. Kapitanov, V. Zeninari, B. Parvitte, D. Courtois and Yu. N. Ponomarev, "Sub-ppm multi-gas photoacoustic sensor", *Spectrochim. Acta A* **63**, 899, 2006.

[32] V. Koskinen, J. Fonsen, J. Kauppinen and I. Kauppinen, "Extremely sensitive trace gas analysis with modern photoacoustic spectroscopy", *Vibr. Spectrosc.* **42**, 239, 2006.

[33] P. Sievilä, V-P. Rytkönen, O. Hahtela, N. Chekurov, J. Kauppinen and I. Tittonen, " Fabrication and characterization of an ultrasensitive acousto-optical cantilever", *J. Microcmech. Microeng.* **17**, 852, 2007.

[34] M. H. de Paula, A. A. de Carvalho, C. A. Vinha, N. Cella and H. Vargas, "Optical microphone for photoacoustic spectroscopy", *J. Appl. Phys.* **64**, 3722, 1988.

[35] V. A. Kapitanov, V. Zeninari, B. Parvitte, D. Courtois and Yu. N. Ponomarev, "Optimisation of photoacoustic resonant cells with commercial microphones for diode laser gas detection", *Spectrochim. Acta A* **58**, 2397, 2002.

[36] N. Bilaniuk, "Optical microphone transduction techniques", *Appl. Acoust.* **50**, 35, 1997.

[37] G. Benedetto, R. Gavioso and R. Spagnolo, "Measurement of microphone membrane displacement with an optical beam deflection technique", *Rev. Sci. Instrum.* **66**, 5563, 1995.

[38] S. M. Park and G. J. Diebold, "Interferometric microphone for photoacoustic spectroscopy", *Rev. Sci. Instrum.* **58**, 772, 1987.

[39] J. Breguet, J. P. Pellaux and N. Gisin, "Photoacoustic detection of trace gases with an optical microphone", *Sens. Actuators A* **48**, 29, 1995.

[40] K. Jasek, B. Mazurek and M. Pasternak, "Frequency characteristics of an optopneumatic detector", *Molecular and Quantum Acoustics* **28**, 131, 2007.

[41] A. A. Kosterev, Yu. A. Bakhirkin, R. F. Curl and F. K. Tittel, "Quartz-enhanced photoacoustic spectroscopy", *Opt. Lett.* **27**, 1902, 2002.

[42] A. A. Kosterev, Y. A. Bakhirkin and F. K. Tittel, "Ultrasensitive gas detection by quartz-enhanced photoacoustic spectroscopy in the fundamental molecular absorption bands region", *Appl. Phys. B* **80**, 133, 2005.

[43] Q. Munir and H. P. Weber, "Fiberoptic sensor in a resonant optoacoustic cell", *Opt. Commun.* **52**, 269, 1984.

[44] J. Kauppinen, T. Kuusela, P. Malmi and J. Raittila, "Brownian noise of the interferometric cantilever microphone used in photoacoustic trace gas detectors", *Pittcon 2009 Book of Abstracts,* Chicago, USA, 2009.

[45] F. Gittes and C. F. Schmidt, "Thermal noise limitations of micromechanical experiments", *Eur. Biophys. J.* **27**, 75, 1998.

[46] J. M. Rey and M. W. Sigrist, "New differential mode excitation scheme for near-infrared water vapour sensing", *Sens. Actuators B* **135**, 161, 2008.

[47] J. M. Langridge, T. Laurila, R. S. Watt, R. L. Jones, C. F. Kaminski and J. Hult, "Cavity enhanced absorption spectroscopy of multiple trace gas species using a supercontinuum radiation source", *Opt. Expr.* **16**, 10178, 2008.

[48] A. Miklós, P. Hess and Z. Bozóki, "Application of acoustic resonators in photoacoustic trace gas analysis and metrology", *Rev. Sci. Instrum.* **72**, 1937, 2001.

[49] A. Grossel, V. Zeninari, L. Joly, B. Parvitte, D. Courtois and G. Durry, "New improvements in methane detection using a Hemholtz resonant photoacoustic laser sensor: A comparison between near-IR diode lasers and mid-IR quantum cascade lasers", *Spectrochim. Acta A* **63**, 1021, 2006.

[50] M. E. Webber, M. Pushkarsky and C. K. N. Patel, "Fiber-amplifier-enhanced photoacoustic spectroscopy with near-infrared tunable diode lasers", *Appl. Opt.* **42**, 2119, 2003.

[51] T. Laurila, H. Cattaneo, T. Pöyhönen, V. Koskinen, J. Kauppinen and R. Hernberg, "Cantilever-based photoacoustic detection of carbon dioxide using a fiber-amplified diode laser", *Appl. Phys. B* **83**, 285, 2006.

[52] V. Koskinen, J. Fonsen, K. Roth and J. Kauppinen, "Cantilever enhanced photoacoustic detection of carbon dioxide using a tunable diode laser source", *Appl. Phys. B* **86**, 451, 2007.

[53] A. M. Parkes, K. A. Keen and E. D. McNaghten, "Trace gas detection using a novel cantilever-based photoacoustic spectrometer with multiplexed optical fiber-coupled diode lasers and fiber-amplification", *Proceedings of SPIE –Fiber Optic Sensors and Applications V*, Eric Udd, (Ed.), vol. 6770, 67701C, 2007.

[54] T. Laurila, H. Cattaneo, V. Koskinen and J. Kauppinen, "Diode laser-based photoacoustic spectroscopy with interferometrically-enhanced cantilever detection", *Opt. Expr.* **13**, 2453, 2005.

[55] H. Cattaneo, T. Laurila and R. Hernberg, "Photoacoustic detection of oxygen using cantilever enhanced technique", *Appl. Phys. B* **85**, 337, 2006.

[56] W. Einfeld, *Environmental Technology Verification Report, Photoacoustic Spectrophotometer, Innova AirTech Instruments Type 1312 Multi-gas Monitor*, U.S. Environmental Protection Agency (EPA), EPA/600/R-98/143, 1998.

[57] J. Fonsen, V. Koskinen, K. Roth and J. Kauppinen, "Dual cantilever enhanced photoacoustic detector with pulsed broadband IR source", article in press, *Vibr. Spectrosc.*, 2009.

[58] M. Wolff and H. Harde, "Photoacoustic spectrometer based on a Planckian radiator with fast time response", *Infrared Phys. Tech.* **44**, 51, 2003.

[59] A. A. Kovalyov and N. R. Klebleyev, "Resonant optoacoustic detector in nondispersive gas analyzer scheme", *Infrared Phys. Technol.* **38**, 415, 1997.

[60] E. Aidam and J. Weinell, *Two-Beam Gas Analyzer and Method for Calibrating a Two-Beam Gas Analyzer*, US Patent 5764354, 1998.

[61] *EL6010-Uras14 Infrared Analyzer Unit*, datasheet 10/24-3.10 EN, www.abb.com/analytical/ (available online December 15th 2008).

[62] L. Kimmig, P. Krause, M. Ludwig and K. Schmidt, *Non-Dispersive Infrared Gas Analyzer*, US Patent 6166383, 2000.

[63] K. Schjølberg-Henriksen, A. Ferber, S. Moe, D. T. Wang, R. W. Bernstein, H. Rogne, O. Schulz, G. Müller, M. Lloyd, and K-H. Suphan, "Sensitive and selective photo acoustic gas sensor suitable for high volume manufacturing", *5th IEEE Conference on Sensors*, 2007.

[64] J. M. Rey and M. W. Sigrist, "Simultaneous dual-frequency excitation of a resonant photoacoustic cell", *Infrared Phys. Technol.* **51**, 516, 2008.

[65] T. Chen, G. Su and H. Yuan, "In situ gas filter correlation: photoacoustic CO detection method for fire warning", *Sens. Actuators B* **109**, 233, 2005.

[66] P. Middleton, "Gas filter correlation techniques", *Internet J. Vib. Spec.* **5**, 6, 2001. (www.ijvs.com)

[67] P. Chambers, *A Study of a Correlation Spectroscopy Gas Detection Method*, thesis, University of Southampton, Southampton, UK, 2005.

[68] L. S. Rothman et al., "The HITRAN molecular spectroscopic database and hawks (HITRAN atmospheric workstation): 1996 edition", *J. Quant. Spectrosc. Radiat. Transfer.* **60**, 665, 1998.

[69] P. L. Meyer and M. W. Sigrist, "Atmospheric pollution monitoring using CO_2 –laser photoacoustic spectroscopy and other techniques", *Rev. Sci. Instrum.* **61**, 1779, 1990.

[70] P. Griffiths and J. A. De Haseth, *Fourier Transform Infrared Spectrometry*, 2nd Edition, John Wiley & Sons, Inc., Hoboken, New Jersey, 2007.

[71] A. Olafsson, G. I. Hansen, A. S. Loftsdottir and S. Jakobsson, "FT-IR photoacoustic trace gas detection", in *Photoacoustic and Photothermal Phenomena: 10th Interntional Conference*, F. Scudieri and M. Bertolotti (Eds.), 208, 1999.

[72] R. S. Wright, G. B. Howe and R. K. M. Jayanty, "Evaluation of a portable Fourier transform infrared gas analyzer for measurement of air toxics in pollution preventionresearch", *J. Air & Waste Manage. Assoc.* **48**, 1077, 1998.

[73] G. Busse and B. Bullemer, "Use of the opto-acoustic effect for rapid scan Fourier spectroscopy", *Infrared Phys.* **18**, 631, 1978.

[74] D. P. Baldwin, R. W. Jones and J. F. McClelland, "Exploration of FTIR-based PAS for on-site analysis of volatile contaminants in air", in *Photoacoustic and Photothermal Phenomena III*, D. Bićanić (Ed.), Springer Verlag, Heidelberg, 3,1992.

[75] J. Kauppinen and J. Partanen, *Fourier Transforms in Spectroscopy*, Wiley-VCH Verlag GmbH, 2001.

[76] J. F. McClelland, S. J. Bajic, et al., *Introduction to Photoacoustic Spectroscopy with Step-Scan and Constant Velocity Scan FTIR Spectrometers*, MTEC Photoacoustics, Inc., 1996.

[77] I. Salomaa, *Analysis and Compensation of Spectral Distortions Encountered in Two-Beam Interferometry*, thesis, University of Turku, Turku, Finland, 1999.

[78] M. Ahro and J. Kauppinen, "Non-linearity of Beer's law in gas phase FT-IR spectroscopy", *Appl. Spectrosc.* **55**, 50, 2001.

[79] I. Johansen, G. Lines, A. Honne and T. Midtgaard, "Calibration of an FT-IR spectrometer for ambient air monitoring by PLS", *Appl. Spectrosc.* **51**, 1540, 1997.

[80] P. Saarinen and J. Kauppinen, "Multicomponent analysis of FT-IR spectra", *Appl. Spectrosc.* **45**, 953, 1991.

[81] D. M. Haaland and E. V. Thomas, "Partial least-square methods for spectral analysis", *Anal. Chem.* **60**, 1193, 1988.

[82] R. Kramer, *Chemometric Techniques for Quantitative Analyses*, Marcel Dekker, New York, 1998.

[83] P. Jaakkola, J. D. Tate, M. Paakkunainen, J. Kauppinen and P. Saarinen, "Instrumental reolution considerations for FT-IR gas phase spectrometry", *Appl. Spectrosc.* **51**, 1159, 1997.

[84] R. O. Carter," The application of linear PA/FT-IR to polymer-related problems" *Appl. Spectrosc.* **46**, 219, 1992.

[85] J. F. McClelland, "Linearization and signal recovery in photoacoustic infrared spectroscopy", *Rev. Sci. Instrum*. **78**, 051301, 2007.

[86] *MTEC Model 300 Photoacoustic Cell Instrument Manual*, MTEC Photoacoustics Inc., 2005. (www.mtecpas.com)

[87] A. Rogalski, *Infrared Detectors*, CRC Press, 149, 2000.